

MINDS: The molecule-rich disc of the Herbig star HD 35929 revealed with JWST/MIRI

Till Kaeufer^{1*}, Rens Waters^{2,3}, Danny Gasman⁴, Milou Temmink⁵, Hyerin Jang², Ewine F. van Dishoeck^{5,6}, Manuel Güdel^{7,8}, Thomas Henning⁴, Alessio Caratti o Garatti⁹, Inga Kamp¹⁰, Aditya M. Arabhavi¹⁰, Pacôme Esteve¹¹, Sierra L. Grant¹², Jayatee Kanwar¹³, Nicolas T. Kurtovic⁶, Giulia Perotti^{14,4}, Kamber Schwarz⁴, Lucas M. Stapper⁴, and Benoît Tabone¹¹

¹*Department of Physics and Astronomy, University of Exeter, Exeter EX4 4QL, UK*

²*Department of Astrophysics/IMAPP, Radboud University, PO Box 9010, 6500 GL Nijmegen, The Netherlands*

³*SRON Netherlands Institute for Space Research, Niels Bohrweg 4, NL-2333 CA Leiden, The Netherlands*

⁴*Max-Planck-Institut für Astronomie (MPIA), Königstuhl 17, 69117 Heidelberg, Germany*

⁵*Leiden Observatory, Leiden University, PO Box 9513, 2300 RA Leiden, The Netherlands*

⁶*Max-Planck Institut für Extraterrestrische Physik (MPE), Giessenbachstr. 1, 85748, Garching, Germany*

⁷*Dept. of Astrophysics, University of Vienna, Türkenschanzstr. 17, A-1180 Vienna, Austria*

⁸*ETH Zürich, Institute for Particle Physics and Astrophysics, Wolfgang-Pauli-Str. 27, 8093 Zürich, Switzerland*

⁹*INAF – Osservatorio Astronomico di Capodimonte, Salita Moiarello 16, 80131 Napoli, Italy*

¹⁰*Kapteyn Astronomical Institute, Rijksuniversiteit Groningen, Postbus 800, 9700AV Groningen, The Netherlands*

¹¹*Université Paris-Saclay, CNRS, Institut d’Astrophysique Spatiale, 91405, Orsay, France*

¹²*Earth and Planets Laboratory, Carnegie Institution for Science, 5241 Broad Branch Road, NW, Washington, DC 20015, USA*

¹³*Department of Astronomy, University of Michigan, 1085 S. University, Ann Arbor, MI 48109, USA*

¹⁴*Niels Bohr Institute, University of Copenhagen, NBB BA2, Jagtvej 155A, 2200 Copenhagen, Denmark*

Accepted 2025 November 17. Received 2025 October 31; in original form 2025 September 5

ABSTRACT

Our knowledge of the chemical composition of the gas in the inner disc of intermediate-mass young stars is limited, due to the lack of suitable instrumentation. The launch of JWST has provided a significant improvement in our ability to probe gas in these inner discs. We analyse the gas composition and emitting conditions of the disc around HD 35929, a young intermediate-mass Herbig star, using MIRI/MRS data. Our goal is to constrain the chemistry and kinematics of the gas phase molecules detected in the inner disc. We use iSLAT to examine the observed molecular lines and DuCKLiNG to detect, fit, and analyse the molecular emission. We find gas phase H₂O, CO, CO₂, and OH in the disc, as well as HI recombination lines. Surprisingly, we also detect gas phase SiO in the fundamental $v=1-0$ vibrational band. We derive column densities and temperature ranges of the detected species, arising from the inner ~ 0.2 au, hinting towards a compact and very warm disc. The molecular column densities are much higher than found in lower mass T Tauri discs. In general, the molecular composition is consistent with an O-rich gas from which silicate-rich solids condense and the strong gas phase molecular line emission suggests a low dust opacity. The unexpected detection of gas phase SiO at the source velocity points to an incomplete condensation of rock forming elements in the disc, suggesting chemical disequilibrium and/or an underestimate of the gas kinetic temperature.

Key words: protoplanetary discs – infrared: general – techniques: spectroscopic – methods: data analysis

1 INTRODUCTION

Herbig Ae/Be stars (hereafter referred to as Herbig stars) (Herbig 1960) are intermediate-mass (1.5 to $\sim 8 M_{\odot}$) pre-main-sequence (PMS) stars surrounded by a planet forming disc (for a recent review, see Brittain et al. 2023). Herbig stars represent a relatively old (a few to 10 Myrs) population of PMS stars, as their spectral types are between B and F (Vioque et al. 2018). Nevertheless, compared to lower mass T Tauri stars, their disc masses are higher (Stapper et al.

2025a). The younger counterparts to Herbig stars are the intermediate mass T Tauri stars (Calvet et al. 2004; Vægård et al. 2021).

Because of their brightness, Herbig star discs have been studied extensively. While atomic emission lines are frequently detected in UV, optical and infrared spectra (e.g., HI Balmer lines, [OI]), little is known about the molecular gas composition of the inner disc. Previous studies using the Infrared Space Observatory (ISO) and the Spitzer Space Telescope showed that the mid-infrared (mid-IR) spectra of Herbig stars are characterized by strong dust emission from amorphous and crystalline silicates, and by Polycyclic Aromatic Hydrocarbons (e.g., Malfait et al. 1998; Meeus et al. 2001; Juhász

* E-mail: t.kaeufer@exeter.ac.uk

et al. 2010; Acke et al. 2010). However, Herbig star discs often lack the molecular line emission that characterizes the mid-IR spectra of lower mass T Tauri stars (e.g. Pontoppidan et al. 2010). This has been attributed to the bright mid-IR to far-IR continuum emission from the disc, which hampers the detection of weak emission lines at low spectral resolution (Antonellini et al. 2015; Antonellini 2016). Also, the strong UV field of warm Herbig stars may photodissociate molecules in the disc (Fedele et al. 2011).

In the 1 to 5 μm wavelength range, Herbig discs regularly show CO ro-vibrational line emission when observed at high spectral resolution (e.g. Brittain et al. 2007). The CO is excited both thermally as well as through IR pumping and UV fluorescence, and originates both from the innermost disc regions, close to the dust sublimation radius (thermal excitation and IR pumping, Blake & Boogert 2004), and from the outer disc surface (UV fluorescence). The inner disc CO emission is correlated with disc geometry as noted by (van der Plas et al. 2008): discs classified as Group I (Meeus et al. 2001), which show large gaps and dust-depleted inner discs, have large inner radii of CO ro-vibrational line emission. In contrast, Group II discs have no large gaps and can show much smaller CO emitting inner radii, that coincide with the dust inner radius; these discs may show smaller, inner disc gaps at spatial scales of a few au (Menu et al. 2015). Hein Bertelsen et al. (2016) show through modeling that the disc geometry affects the CO line widths, providing a tool to constrain disc structure. Banzatti et al. (2018, 2022) noted that the CO inner radius increases when the near-IR excess decreases. This is consistent with a picture in which the inner radius of CO increases as dust in the inner disc, or the inner disc surface layer, is depleted. A small group of Herbig stars, including HD 35929, shows CO first overtone emission, indicative of a very hot and dense inner disc molecular reservoir (Ilee et al. 2014). In addition to CO, both H₂O and OH have been detected in Herbig star discs at near-IR wavelengths (Fedele et al. 2011; Adams et al. 2019; Banzatti et al. 2023). OH emission was found to occur more frequently in Group I discs (Brittain et al. 2016). In only one Herbig star, HD 101412, CO₂ was detected using *Spitzer* (Pontoppidan et al. 2010).

The launch of the James Webb Space Telescope (JWST) has opened the possibility to search for weak mid-IR molecular gas line emission arising from the inner regions of planet forming discs. Initial results show a wide diversity in the inner disc chemistry, with molecules as H₂, CO, H₂O, CO₂, OH, C₂H₂, and HCN commonly detected in solar mass T Tauri discs, while a rich variety of hydrocarbons has been found in discs surrounding lower mass (< 0.2-0.3 M_⊙) objects (e.g. Perotti et al. 2023; Grant et al. 2023b; Arabhavi et al. 2024; Pontoppidan et al. 2024; Colmenares et al. 2024; Arabhavi et al. 2025; Temmink et al. 2025; Arulanantham et al. 2025). Most well-studied Herbig stars are too bright for JWST/MIRI. For that reason, only four Herbig stars were included in the MIRI mid-InfraRed Disk Survey (MINDS, Kamp et al. 2023; Henning et al. 2024) program. Here we present the MIRI spectrum of one of these, HD 35929. This paper is organised as follows: in Section 2 we discuss the observation and its context. This includes the properties of HD 35929 and its evolutionary stage (Sect. 2.1), the data reduction of the JWST/MIRI data (Sect. 2.2), the inventory of atoms, molecules, and dust identifiable by eye (Sect. 2.3), and the kinematic information from spectrally resolved lines (Sect. 2.4). Section 3 describes a modelling approach to analyse the data (introduced in Sect. 3.1) with the results of the fitting described in Section 3.2. In Section 4 we discuss the implications of our findings. Finally, Section 5 contains the conclusions of this study.

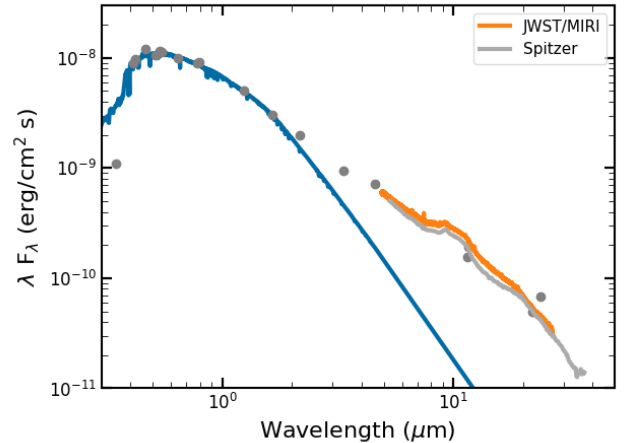


Figure 1. Spectral Energy Distribution of HD 35929. The blue curve is a Kurucz model with $T_{\text{eff}} = 6500$ K and $\log g = 3.5$, reddened with $A_V = 0.20$ mag. The orange and grey lines represent the JWST/MIRI and Spitzer/IRS spectra, respectively. Also shown are photometric points (Strömgren, GAIA, 2MASS, IRAC, WISE, and IRAS).

2 AN OBSERVATIONAL PERSPECTIVE

2.1 Properties of HD 35929

HD 35929 is an F2 IV-V star located in the direction of the Orion OB1 association. The distance of 380 pc (Gaia Collaboration 2020) places it firmly in the Orion star-forming region. In the HR diagram, the star is located above the main sequence (Fairlamb et al. 2015; Vioque et al. 2018; Valegård et al. 2021). These studies used PMS evolutionary tracks to constrain the stellar mass and age to 2.9 M_⊙ and 1.1-1.7 Myrs, respectively. From optical spectroscopy, an effective temperature of 7000 K has been inferred, and a metallicity of [Fe/H] = -0.2 (Miroshnichenko et al. 2004). However, we note that the GAIA derived temperature is only 6400 K, which would imply a significantly lower [Fe/H] of ~ -0.4 . We have used the ARIADNE software tool (Vines & Jenkins 2022) to fit the stellar Spectral Energy Distribution (SED), shown in Fig. 1. Fitting a grid of Kurucz model atmospheres (Kurucz 1979) to these data results in a temperature of 6500 K, a stellar radius of 6.7 R_⊙ and a luminosity of 74 L_⊙, in good agreement with previous studies, and would suggest a metallicity of [Fe/H] of about -0.4. Miroshnichenko et al. (2004) suggested that HD 35929 is a post-main-sequence star rather than a young PMS star. Unfortunately, post- and pre-main sequence evolutionary tracks intersect in this part of the HR diagram, which therefore cannot help to distinguish post- and pre-main-sequence stars. We note that HD 35929 is not closely associated with a cluster in Orion (Vioque et al. 2023), and that it is classified as a δ Scuti pulsating star (Marconi et al. 2000) of the γ Dor class (Barceló Forteza et al. 2020).

The SED (Fig. 1) shows that the IR excess of HD 35929 is modest compared to other Herbig stars, and the very steep negative slope of the IR continuum classifies it as a Group II disc. Stapper et al. (2025b) using ALMA find a dust mass in HD 35929 of 0.23 M_⊙ and an upper limit to the disc radius of 17 au. The gas accretion rate onto HD 35929 has been measured using different diagnostics (Fairlamb et al. 2015; Grant et al. 2022; Ilee et al. 2014; Wichittanakom et al. 2020), leading to mass accretion rates between $10^{-6.8}$ and $10^{-6.31}$ M_⊙yr⁻¹. Adopting the canonical gas-to-dust ratio of 100, this leads to an unrealistic short disc lifetime of a 3-4 years. We will return to this point in Sect. 4.2. Grady et al. (1996) report Type III P Cygni

emission line profiles in the MgII 2802.7 Å, 2795 Å lines as well as strong emission from CIV and OI. Valenti et al. (2000) report far-UV line emission from SI, OI, and SiII.

Near-IR ro-vibrational line emission from CO in the fundamental $v=1-0$ and $v=2-0$ overtone bands has been detected (Ilee et al. 2014; Banzatti et al. 2022), pointing to a compact rotating ring of dense gas with high densities and high column densities, probably from a dust-free region with a radius of 0.21 au, well inside the dust sublimation radius (estimated at 0.4 au, Banzatti et al. 2022). The *Spitzer* IRS spectrum of HD 35929 shows weak silicate emission, dominated by large ($2 - 5 \mu\text{m}$) amorphous grains with SiO₂, SiO₃ and SiO₄ composition (Juhász et al. 2010), while no evidence for 0.1 μm sized amorphous silicates was found. The absence of small grains suggests a low dust opacity, possibly exposing more gas above the optically thick dust layers. Lazareff et al. (2017) marginally resolve the inner disc in the H band using Pionier at the Very Large Telescope Interferometer (VLTI) and find a size of ~ 0.21 au, and a poorly constrained disc inclination angle of 31.8 ± 16 degrees.

2.2 Observations and data reduction

HD 35929 was observed with JWST/MIRI (Wright et al. 2023; Argriou et al. 2023) as part of the MINDS GTO program. The observation used a point source positive dither pattern without target acquisition, for a duration of approximately 22 minutes per band. The data were reduced using version 1.16.1 of the standard JWST pipeline (Bushouse et al. 2024). The fringes were corrected using both the CALWEBB_SPEC2 fringe flat and residual fringe correction steps, along with a final residual fringe correction on the extracted spectrum. The spectrum was extracted per band from the cube images, using a double the Full Width at Half Maximum (FWHM) circular aperture and an annulus to estimate the background. The pipeline outlier detection step was applied, and outliers were replaced using the pixel_replace option in CALWEBB_SPEC3. Because the spectrum is full of emission lines, an estimate of the flux uncertainties was difficult to make. The S/N of the data, derived from the MIRI pipeline, ranges between ~ 100 and ~ 800 (for the wavelength range up to 25 μm).

2.3 Atomic, molecular and dust inventory

The MIRI spectrum shown in Fig. 2 is dominated by thermal emission from warm silicate grains in the disc. The 10 μm silicate band shows a narrow peak near 9.2 μm , often associated with silicates with an SiO₂ composition (Sargent et al. 2008). Superimposed is prominent emission from ro-vibrational lines of H₂O, and at longer wavelengths many weaker H₂O rotational lines. Other molecules that can easily be identified are CO $v=1-0$, $v=2-1$ and $v=3-2$ P branch emission (Fig. A1 in Appendix A), SiO $v=1-0$, the CO₂ bending mode branch at 14.98 μm and pure rotational lines of OH. We do not find evidence for H₂ line emission. To our knowledge, this is the first detection of gas phase SiO vibrational line emission in a disc orbiting an intermediate-mass young star. Therefore, Sect. 3.2.1-3.2.3 highlight the robustness of this detection. In addition, a number of HI recombination lines are detected, as well as the [FeII] λ 17.395 μm fine structure line. The JWST/MIRI and *Spitzer*/IRS spectra (Fig. 2) show 5-25 percent differences in continuum flux, that are likely larger than calibration uncertainties. The ro-vibrational water band near 6.5 μm is clearly visible in both datasets. We note that the persistent disc emission between the *Spitzer* and JWST/MIRI epochs, separated by 2 decades, is inconsistent with the disc lifetime mentioned above. In the next

sections, we will describe how we quantify the gas emission from the disc starting with the line kinematics in Sect. 2.4.

2.4 Emission line kinematics

The large line widths ($\sim 100 \text{ km s}^{-1}$) of the double-peaked CO ro-vibrational lines in HD 35929 reported by Banzatti et al. (2022) suggest that CO is in a rotating gaseous disc observed at a non-zero inclination, consistent with the inclination inferred by Lazareff et al. (2017). Therefore, the molecules and atomic lines detected in the MIRI data at much lower spectral resolution may be spectrally resolved (Banzatti et al. 2025). For instance, the 4.9–5.2 μm spectral region indeed shows broad CO lines, while the presence of CO $v=2-1$ and $v=3-2$ hot band emission lines results in significant line blending (Fig. A1). Similar line kinematic broadening and line blending is seen for the other detected molecules. To quantify the kinematics of the gas, we used iSLAT (Jellison et al. 2024) to fit Gaussian line profiles to individual emission lines of molecules and HI gas, avoiding line blends as much as possible. The choice of water lines was based on Banzatti et al. (2025), probing both pure rotational as well as ro-vibrational lines, and different excitation levels. We accounted for the instrumental spectral resolution given by Pontoppidan et al. (2024).

The results are listed in Table E1 (Appendix E). We show the instrument corrected FWHM as a function of the Doppler shift in Fig. 3, where we applied a stellar heliocentric radial velocity of 22 km s^{-1} (H. van Winckel, private comm.). It is clear that the emission lines are spectrally resolved, consistent with line widths obtained from ground-based high spectral resolution observations by Banzatti et al. (2022). We find FWHM values between ~ 50 and $\sim 300 \text{ km s}^{-1}$, but many lines are clustered near $\sim 130 - 140 \text{ km s}^{-1}$, with a tail towards higher values. We cannot exclude the possibility that some of the broader lines are still affected by blends, and the lower range of FWHM is more likely to represent the actual kinematic broadening. This is supported by the width of the strongest HI lines, whose width is not affected much by any molecular line contribution (Table E1), and by the spectrally resolved $v=1-0$ CO lines reported by Banzatti et al. (2022) that show a FWHM of 125 km s^{-1} . The FWHM of the emission lines is similar for different molecular species as well as for the HI lines, and does not depend on the upper level energy or the wavelength of the transition. This suggests that the line emitting region is similar for all species. The median Doppler shift of the lines is $-4 \pm 36 \text{ km s}^{-1}$; taking only lines with a FWHM less than 200 km s^{-1} , this becomes $-2 \pm 13 \text{ km s}^{-1}$. This small non-zero value shows that the bulk of the gas is not flowing out or accreting, and is consistent with rotational broadening. Finally, we mention the [FeII] fine structure line observed at 17.9372 μm , with a FWHM of $161 \pm 12 \text{ km s}^{-1}$ at a velocity of $-60 \pm 5 \text{ km s}^{-1}$.

The large line widths imply that the (molecular) gas must be close to the star. Lazareff et al. (2017) derive an uncertain disc inclination angle of 31.8 ± 16 degrees. Assuming a typical projected rotational velocity of 65 km/s, and adopting the stellar parameters given in Section 2.1, this corresponds to a distance scale of 0.17 au or 5.3 R_* . This is roughly consistent with the spatial scale of Bry emission detected in Herbig stars (GRAVITY Collaboration et al. 2019). We conclude that the gas is located close to, or inside the dust sublimation distance of 0.4 au. Next, we further analyse the gas emission using 1D modelling.

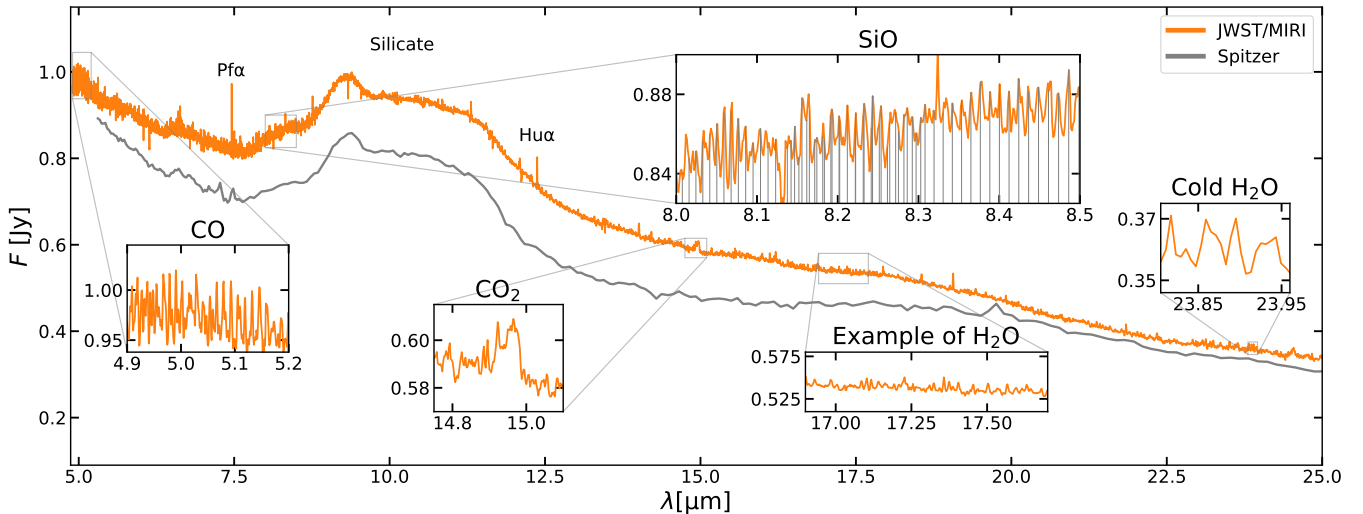


Figure 2. JWST/MIRI MRS spectrum (orange) of HD 35929. The Spitzer/IRS spectrum (grey) is shown for comparison. The insets highlight the emission from CO, CO₂, H₂O, and most notably the SiO fundamental vibrational mode. The vertical lines in the SiO panel indicate the positions of the rotational lines with upper level energies lower than 3600 K.

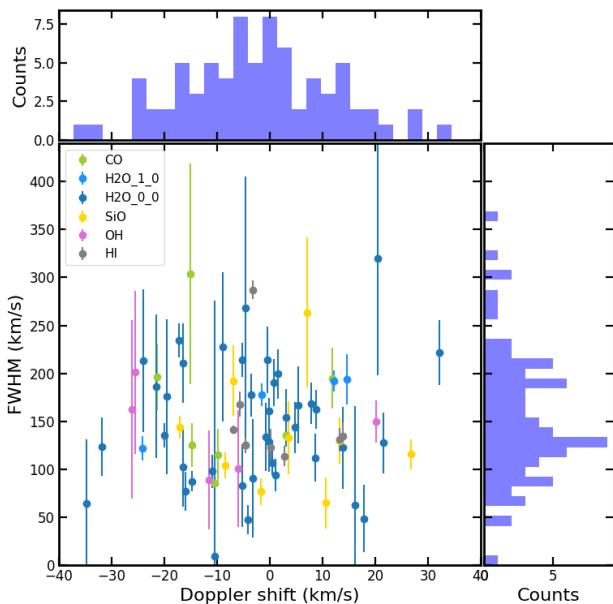


Figure 3. Full Width at Half Maximum line widths of selected emission lines as a function of their Doppler shift. A stellar radial velocity of 22 km s^{-1} was adopted.

3 A MODELLING PERSPECTIVE

3.1 Fitting process

We fitted the JWST/MIRI-MRS spectrum of HD 35929 using the Dust Continuum Kit with Line Emission from Gas (DuCKLinG¹, Kaeufer et al. 2024a). While DuCKLinG has the capability of simultaneous fitting both for the gas and dust composition (e.g. Kaeufer et al. 2024a,b), in this study, we focus on the gas emission and defer

an analysis of the dust mineralogy to a subsequent study. Therefore, the gas emission of the JWST/MIRI spectrum is isolated using the method introduced by Temmink et al. (2024a), resulting in the continuum-subtracted spectrum shown in Fig. 4. In addition, we selected two wavelength windows that show the strongest molecular emission ($4.9 - 9.0 \mu\text{m}$ and $13.5 - 25 \mu\text{m}$). These regions are highlighted in Fig. 4. We excluded the region around the silicate feature ($9.0 - 13.5 \mu\text{m}$) from the fit due to poor fitting quality in this region which might originate from unaccounted molecular emission.

The continuum-subtracted spectrum is analysed using DuCKLinG’s gas component (fitting all examined molecules simultaneously), which is described in detail by Kaeufer et al. (2024a). In brief, this component is based on a large grid (in column density and temperature) of 0D local thermodynamic equilibrium (LTE) slab models (as introduced by Tabone et al. 2023; Arabhavi et al. 2024) that can be interpolated and integrated to mimic the emission along a radial temperature and column density power law or can be used to obtain the flux for models with single values for both quantities. The total gas emission is simply the sum of all molecular fluxes (accounting for line overlap for each molecule but not between molecules). We note that the SiO slab models use molecular line data from the ExoMol database (Buldyreva et al. 2022; Guest et al. 2024; Tennyson et al. 2024), while the others are based on HITRAN (Gordon et al. 2022). The slab models are similar to those used in other studies using JWST/MIRI-MRS observations of planet-forming discs of the MINDS, XUE and JDISCS programs. In this study, we convolved all slab models with the spectral resolution of JWST/MIRI-MRS limited to values not larger than $R = 2500$ (for $\lambda < 18.0 \mu\text{m}$ $R = 2500$ and $R = 2000$ beyond that). This accounts for the fact that the spectrum of HD 35929 shows significant rotational broadening (Sect. 2.4). Additionally, the radial velocity of HD 35929 of 22 km s^{-1} is high enough to leave a visible shift on the observed spectrum. Therefore, we shift the observed spectrum to its rest frame before comparing it to models, which are rebinned to the observed wavelength points using the SpectRes Python package (Carnall 2017).

We fitted the observation using MultiNest (Feroz & Hobson 2008; Feroz et al. 2009, 2019) through the Python interface PyMultiNest (Buchner et al. 2014). This Bayesian inference tool uses multimodal

¹ <https://github.com/tillkaeufer/DuCKLinG>

nested sampling to determine the Bayesian evidence and posterior distribution for a given likelihood function. The details about the algorithm and the numerical implementation are described in the provided references above.

The fitting quality is determined using a Gaussian likelihood function \mathcal{L} that evaluates the difference between model flux ($F_{i,\text{model}}$) and observed flux ($F_{i,\text{obs}}$) with respect to the given uncertainty σ_i per data point i with a given weight (w_i) for all wavelengths points (N_{obs})

$$\mathcal{L} = \prod_{i=1}^{N_{\text{obs}}} \left[\frac{1}{\sqrt{2\pi} \sigma_i} \exp\left(-\frac{(F_{i,\text{model}} - F_{i,\text{obs}})^2}{2\sigma_i^2}\right) \right]^{w_i} \quad (1)$$

As detailed by Kaeufer et al. (2024a), the uncertainty σ_i in this description accounts not just for the observational uncertainty, but also for the mismatch of the model to the observation and is treated as a free parameter (σ , which is wavelength independent) that is optimised during the fitting.

The likelihood function treats every observational point independently, which effectively results in wavelength regions with more points having a greater influence on the resulting likelihood value. To mitigate this effect, we determine a weight for every point. These weights (w_i) are proportional to the difference in wavelength between two consecutive data points in the spectrum with $\sum_i w_i = N_{\text{obs}}$ resulting in an uniform contribution by wavelength to the likelihood function. For the case in which the Bayesian evidence is compared between fits (Sect. 3.2.1 and Sect. 3.2.2), we opted to set all weights to 1 to not influence the evidence calculations, while fits analysing the emitting conditions all follow the weight description above.

Next to the likelihood function, priors need to be defined for all fitted parameters (Table 1). To remain agnostic about the value of the parameters, we choose uniform priors based on the limits of the slab grid created by Arabhavi et al. (2024) when possible. While the maximum ($T_{\text{max}}^{\text{mol}}$) and minimum ($T_{\text{min}}^{\text{mol}}$) temperature parameters for every molecule (mol) use uniform priors in linear space (\mathcal{U}), the large possible variation in column density leads us to choose uniform priors in logarithmic space (\mathcal{J}) for the column density at the maximum ($N_{\text{max}}^{\text{mol}}$) and minimum temperature ($N_{\text{min}}^{\text{mol}}$). For CO₂ and C₂H₂ the upper limit for both column density priors are set to 10^{21} cm^{-2} . This is based on first tests where very optically thick CO₂ and C₂H₂ components were fitted. To exclude these extreme cases, which do not fit any clear molecular features, from our analysis we lowered the upper column density limit for CO₂ and C₂H₂. For SiO the upper column density limit is set to 10^{20} cm^{-2} for the same reason. Similarly, the upper temperature limits for CO were extended to from 1500 K to 2500 K since first tests showed a CO temperature convergence toward the upper temperature limit. The prior of the slope of the radial temperature power law (q_{emis}) is chosen to ensure a radial decrease in temperature and to include extracted slopes from thermochemical models (e.g. Fedele et al. 2016; Brittain et al. 2023). The emitting area of every molecule is not treated as a Bayesian parameter but due to its linear nature optimised with non-negative least square fitting for every parameter combination during the fitting (see Kaeufer et al. 2024a,b). The uncertainty parameter σ includes typical observational uncertainties and could potentially be adjusted if the parameter's posterior distribution converges towards the priors' edges.

3.2 Modelling results

We aim to describe the molecular emission seen in the JWST/MIRI spectrum of HD 35929. For that, we need to first determine which

Table 1. Prior distributions of all free Bayesian parameters. For CO, the temperatures priors are extended up to 2500 K. For CO₂ and C₂H₂, the column density priors range only up to 10^{21} cm^{-2} to avoid extremely optically thick cases. For SiO, the upper limit is set to 10^{20} cm^{-2} for the same reason. The terms $\mathcal{U}(x, y)$ and $\mathcal{J}(x, y)$ denote uniform and log-uniform priors in the range from x to y , respectively.

Parameter	Prior
$T_{\text{max}}^{\text{mol}}$ [K]	$\mathcal{U}(25, 1500)$
$T_{\text{min}}^{\text{mol}}$ [K]	$\mathcal{U}(25, 1500)$
$N_{\text{min}}^{\text{mol}}$ [cm^{-2}]	$\mathcal{J}(10^{14}, 10^{24})$
$N_{\text{max}}^{\text{mol}}$ [cm^{-2}]	$\mathcal{J}(10^{14}, 10^{24})$
q_{emis}	$\mathcal{U}(-2, -0.1)$
σ [mJy]	$\mathcal{J}(0.1, 10)$

molecules are needed and if radial power laws in temperature and column density result in significant improvements of the fitting quality.

3.2.1 Detected gas phase molecules

To evaluate the evidence for different molecules we run Bayesian retrievals (with an evidence tolerance of 0.5) including and excluding individual molecules, following the procedure outlined by Kaeufer et al. (2024b). The evidence for every molecule is calculated by the logarithm of the Bayes factors ($\ln B$) between a run with and without the molecules. The Bayes factor is a measure calculating the differences in global evidence for two fits. Values of $\ln B < 1$, $1 < \ln B < 2.5$, $2.5 < \ln B < 5$, $5 < \ln B < 11$, and $11 < \ln B$ are interpreted as no evidence, weak evidence, moderate evidence, strong evidence, and very strong evidence, respectively, for one model over another (Trotta 2008). The preference of the original model is indicated by a positive sign of $\ln B$. A negative value indicates a preference for the variant model.

We start with a fit including five molecules for which features are visually identified in the spectrum: H₂O, CO, CO₂, SiO, and OH (see Sect. 2.3). This setup is called the original model. We quantify the evidence for these molecules by excluding them (one at a time) from the fit. Additionally, we test the evidence for C₂H₂ and HCN by adding them to the original model. All molecules are treated as OD slabs (no temperature and column density range) for this test to reduce the fit complexity. In this case, the priors for the temperature and column density follow Table 1. The evidence for more complex molecular conditions is tested in Sect. 3.2.2.

The results are listed in Table 2. The logarithm of the Bayes factors is negative for all five runs excluding one of the molecules that were visually identified (H₂O, CO, CO₂, SiO, and OH). The large values ($\ln B \gg 11$) indicate that fits excluding these molecules result in significantly worse residuals, which henceforth is interpreted as strong evidence for their detection.

We include all these molecules in the further fitting process. However, we note that OH is most likely not in LTE contrary to the assumption of the model (e.g. Carr & Najita 2014; Tabone et al. 2024). Therefore, we refrain from interpreting the extracted conditions for OH.

The inclusion of HCN results in an inconclusive Bayes factor ($\ln B = 0.90$), which shows that the inclusion of HCN is not needed to explain the data. Henceforth, we exclude HCN from further fitting.

Similarly, the addition of C₂H₂ does not significantly change the

Table 2. Bayes factors quantifying the evidence for different molecules in the JWST/MIRI spectrum of HD 35929. The first column (Mol.) lists the included or excluded molecule compared to the original model that includes H₂O, CO, CO₂, SiO, and OH. The logarithm of the Bayes factor between the fit with and without a molecule ($\ln B$) indicates if there is a preference (Pref.) for the new fit over the original one. The evidence-column shows the interpretation of $\ln B$ (Trotta 2008).

Mol.	$\ln B$	Pref.	Evidence
w/o H ₂ O	-4456.31	No	Very strong
w/o CO	-1746.55	No	Very strong
w/o CO ₂	-171.61	No	Very strong
w/o SiO	-415.02	No	Very strong
w/o OH	-30.17	No	Very strong
C ₂ H ₂	1.96	Yes	Weak
HCN	0.90	Yes	None

evidence ($\ln B = 1.96$). Since the value of the Bayes factor is slightly larger than the one for HCN, we visually inspected the two fits (with and without C₂H₂). As seen in Fig. 5, the slight improvement in fit quality for the fit including C₂H₂ is not driven by a fitted molecular feature but just by a slightly better match to the noise in the data. Due to the additional component, the water model shifts to slightly different best parameters which explains the flux changes at prominent water lines. Together with the lack of a clearly identifiable *Q*-branch, we conclude that the observation does not hold any proof for a C₂H₂ detection in HD 35929, which is therefore excluded from further fitting.

3.2.2 Molecular complexity

After determining which molecules are visible in the JWST/MIRI spectrum of HD 35929, we analyse the complexity of their emitting conditions (temperature and column density ranges over fixed conditions). Thermochemical models show that some molecules emit lines along an extended surface layer that cannot easily be described by a single temperature and column density (e.g. [Woitke et al. 2024](#); [Kanwar et al. 2025](#)). Therefore, several studies used series of slab models to mimic this behaviour (e.g. [Romero-Mirza et al. 2024](#); [Temminck et al. 2025](#)). We aim to quantify the need for this increase in complexity by following [Kaeufer et al. \(2024b\)](#). Similarly to the detection runs, Bayes factors are used to quantify the evidence for different setups. We start with every molecule as a 0D slab and compare that to fits where individual molecules are treated as temperature power laws or temperature and column density power laws. The Bayes factor between those fits quantifies if the added parameters are justified by a significant increase in fitting quality.

The Bayes factors and their interpretations are listed in Table 3. For SiO, neither the inclusion of a temperature power law nor the additional inclusion of a column density power law significantly increases the quality of the fitting. Therefore, we conclude that the emission of SiO in HD 35929 originates in a region with near-constant conditions. For all other molecules, there is evidence for the inclusion of a column density power law. For OH this evidence is only weak, with no evidence towards a temperature range without a simultaneous addition of a column density range. The evidence for CO increases moderately for a temperature gradient but the addition of a column density power law improves the fit significantly. CO₂ shows similar evidence for the temperature power law with and without a column density range. The strongest evidences can be found for H₂O ($\ln B = 180.12$ and $\ln B = 192.93$). The drastic increase in evidence

Table 3. Bayes factors quantifying the evidence for different model choices in the JWST/MIRI spectrum of HD 35929. The first column (Mol.) lists the molecule for which the complexity is changed compared to the original model. The logarithm of the Bayes factor between the base model and the model with increased complexity ($\ln B$) indicates if there is a preference (Pref.) for the new fit over the original one. The evidence-column shows the interpretation of $\ln B$ (Trotta 2008). The best model shown in the last column includes CO, CO₂, H₂O, and OH with temperature and column density power laws with an additional 0D SiO component.

Mol.	<i>T</i> range	<i>N</i> range	$\ln B$	Pref.	Evidence
CO	Yes	No	3.18	Yes	Moderate
CO	Yes	Yes	13.84	Yes	Very strong
CO ₂	Yes	No	4.73	Yes	Moderate
CO ₂	Yes	Yes	5.61	Yes	Strong
H ₂ O	Yes	No	180.12	Yes	Very strong
H ₂ O	Yes	Yes	192.93	Yes	Very strong
OH	Yes	No	0.30	Yes	None
OH	Yes	Yes	2.46	Yes	Weak
SiO	Yes	No	-0.60	No	None
SiO	Yes	Yes	-0.17	No	None
Best			214.47	Yes	Very strong

for the inclusion of a temperature power law conclusively shows that water is emitting from a range of conditions in discs and is poorly approximated by 0D slab models (consistent with previous studies, e.g. [Romero-Mirza et al. 2024](#); [Temminck et al. 2024b](#)).

Based on these results, we select the best fit which includes column density and temperature power laws for CO, CO₂, H₂O, and OH, while SiO is described by constant column density and temperature. As shown in Table 3, this fit’s Bayes factor ($\ln B = 214.47$ with $w_i = 1$ for all i) is as expected better than all individual complexity enhancements.

3.2.3 Emission contributions and conditions

We run the retrieval with the molecules and the molecular complexities determined in Sect. 3.2.1 and Sect. 3.2.2, respectively. This setup is identical to the ‘Best’ model listed in Table 3, with the inclusion of wavelength-dependent weights (Eq. 1). The modelled flux for this model compared to the observation is shown in Fig. 4. While large parts of the spectrum are very well fitted, at long wavelengths there are several features that the model cannot explain (e.g. around 23.4 μm and 24.5 μm). These might be unaccounted molecular emission or mismatches in the continuum estimation. However, the spectrum is dominated by the emission of water, but clear features of CO and CO₂ are also visible at 5 μm and 15 μm , respectively. Additionally, multiple OH lines appear between 15 μm and 25 μm . While all of these molecules are commonly detected in JWST/MIRI spectra, the detection of SiO is more surprising. The upper panel of Fig. 6 displays a zoom-in to the region dominated by SiO. While the fit is not perfect, it becomes clear that several emission features in the observations are well matched by SiO. To add to the significance of that, we run a fit with H₂O-only to the wavelength region dominated by SiO (7.5 – 9.0 μm) to conclusively show that the emission seen in the observation cannot be explained without SiO. The residual of this fit is compared to the residual of the full fit in the lower panel of Fig. 6. The mean of the absolute values of the residuals are smaller for the full fit (~ 5.11 mJy) compared to the H₂O-only fit (~ 6.43 mJy). Additionally, the latter shows many clear residual lines which are well fitted by SiO in the full fit. Therefore, these lines are most likely due to SiO.

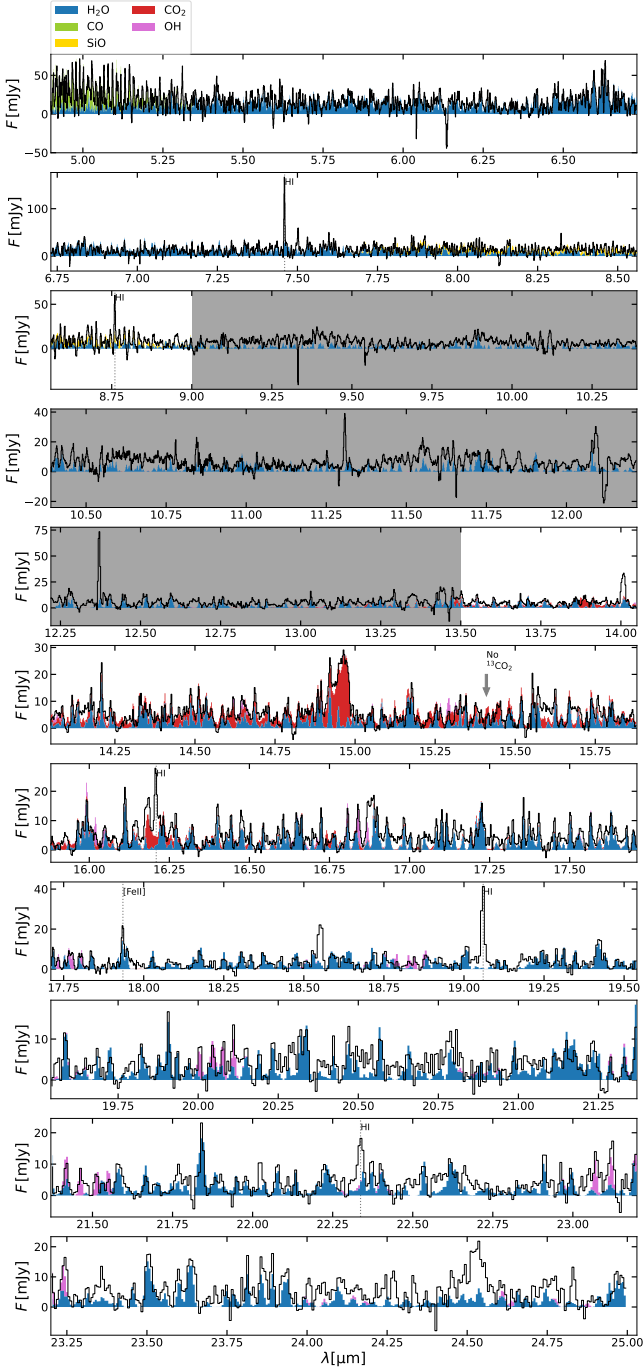


Figure 4. Continuum subtracted MIRI spectrum, using the 4.9 - 25 μm wavelength range, but excluding the 10 μm silicate band region between 9.0 and 13.5 μm (excluded region marked in grey). Overplotted are the cumulative fluxes from H₂O, CO, SiO, CO₂, and OH from the median probability model. A few unfitted atomic lines and the non-detection of ¹³CO₂ are labelled. The apparent feature around 18.55 μm can be traced back to a bad pixel artifact.

Based on this full fit (Fig. 4), we analyse the molecular conditions of the models of the posterior. Fig. 7 shows the posterior distributions of column density and temperature for all fitted molecules (except OH which is excluded due to its non-LTE origin). The coloured regions indicate the full temperature and column density ranges for all posterior models. Additionally, the region which dominates the integrated flux is plotted as contours. For this, the radial cumulative

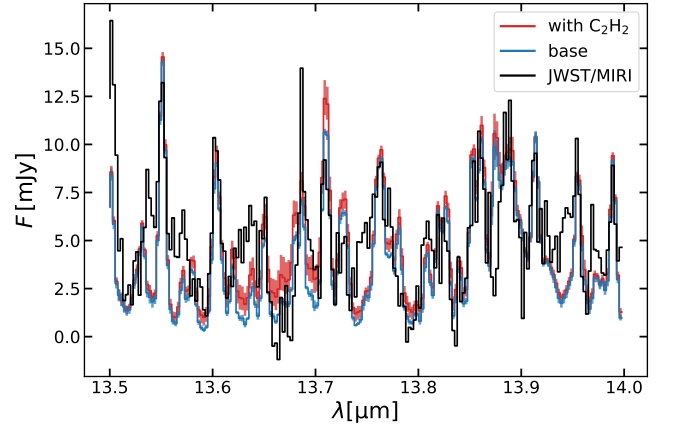


Figure 5. Flux from the base model (blue) and a model including C₂H₂ (red) compared to the observation (black) in the region where C₂H₂ emission is expected. The lines indicate the median posterior flux, with the shaded region indicating the 1 σ level.

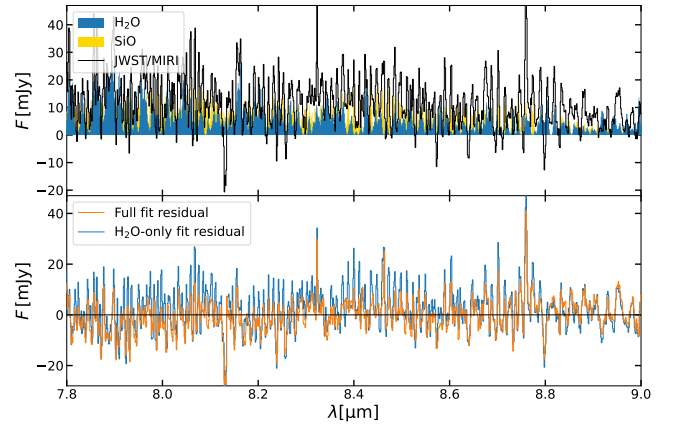


Figure 6. Residual in the wavelength range dominated by SiO of the full fit compared to a water-only fit.

flux per molecule is determined for every model. The radii which enclose 15% and 85% of the cumulative flux are chosen as the inner and outer radius of the effective emitting region, following Kaeufer et al. (2024a) based on typical definitions used by thermochemical models (e.g. Woitke et al. 2024). After deriving this region for every individual model, the distribution of these regions over the full posterior is taken and indicated in Fig. 7.

All molecules show signs of high column densities ($> 10^{18} \text{ cm}^{-2}$), with CO₂ and SiO emitting at column densities of $\sim 10^{19} \text{ cm}^{-2}$ and CO and H₂O emitting from even higher column densities ($> 10^{20} \text{ cm}^{-2}$). Given these high column densities, we searched for isotopologue features in the spectrum (Appendix D), but no clear features were found. CO shows emission from the highest temperatures ($\sim 1500 \text{ K}$ and beyond) hinting towards an origin close to the star, where temperatures are highest. While CO₂ emits from a wide temperature range (from $\sim 250 \text{ K}$ to $\sim 1000 \text{ K}$), the emission of SiO is confined to a narrow temperature range between 500 K and 900 K.

Next to the column density and temperature, we retrieve the emitting area of every molecule. For CO, SiO and CO₂, the emitting area where most of the emission (defined as the range between 15% and 85% of the radial cumulative flux) originates, are equivalent to discs with radii of 0.12 au, 0.22 au, and 0.14 au, respectively. For CO

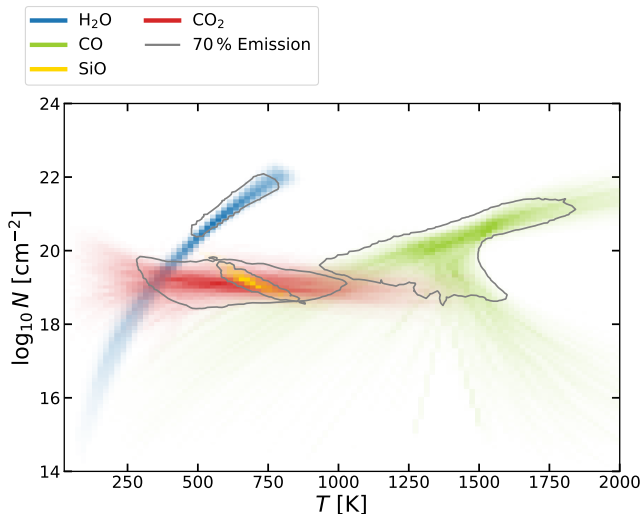


Figure 7. Probability distribution of the molecular column densities and temperatures derived from the continuum subtracted MIRI spectrum. The colours show the emissions for the molecules listed in the legend, while the contours denote the region with the highest contribution to the respective molecular fluxes.

and CO₂, which are fitted with radial profiles these regions extend outwards no more than 0.15 au. Even though these radii are purely based on the derived temperature slope and emitting area, all radial extents are consistent with the close in physical extent of 0.17 au derived by the line kinematics (Sect. 2.4). We caution however that the spatial scales derived from FWHM measurements reflect typical distance scales while the slab models provide radiating surfaces, and so their similarity may be coincidental.

To increase our confidence in the high retrieved column densities, we examined CO₂ and H₂O in more detail. Fitting a narrow wavelength range around the CO₂ Q-branch (14.8 – 15.0 μm) with CO₂ and H₂O results in CO₂ column densities of $\sim 10^{18} \text{ cm}^{-2}$. While this is lower than the value retrieved fitting the full wavelength range ($\sim 10^{19} \text{ cm}^{-2}$), it shows that high column densities for CO₂ are retrieved independently of the exact fitting method. Similarly, we examine water by fitting different wavelength ranges.

The ro-vibrational water lines, which have to be fitted to constrain the SiO properties, contain non-LTE effects, which limits the conclusions drawn from LTE models (Banzatti et al. 2023). Therefore, the rotational water lines are regularly used to analyse the water spectrum observed by JWST/MIRI (e.g. Romero-Mirza et al. 2024; Temmink et al. 2025). To gather a more accurate picture of the emission conditions of water, we repeat the fits presented in Sect. 3.1 for the wavelength range of 13.5 – 25 μm , which excludes the ro-vibrational water. Since this wavelength also excludes CO and SiO emission we exclude these molecules from the fit. All other species are included using temperature and column density power laws. The resulting fit is displayed in Fig. C1 in Appendix C.

We perform an additional fit that is only focused on the unblended rotational water lines determined by Banzatti et al. (2025). For this fit, narrow wavelength windows around each line are selected (based on Table 5 of Banzatti et al. 2025) and water is included as the only molecule. The resulting fit is shown in Fig. C2 in Appendix C.

The extracted emission conditions from the full water fit, the fit of the rotational lines, and the unblended rotational lines are shown in Fig. 8. It can be seen that there is a large overlap between the extracted conditions, albeit with significant spread. In all cases, wa-

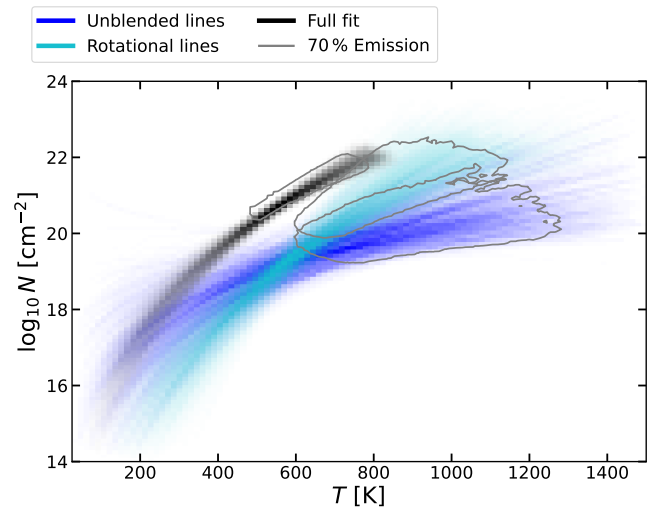


Figure 8. Probability distribution of the molecular column densities and temperatures derived from the fit to the full spectrum (same as water in Fig. 7, black), the rotational water spectrum (cyan), and the unblended rotational lines (bright blue).

ter emits from very large column densities ($> 10^{20} \text{ cm}^{-2}$). This is significantly higher than extracted column densities from T Tauri stars, that typically range between 10^{18} and 10^{20} cm^{-2} (e.g. Temmink et al. 2025). This means that many water lines are optically thick and huge columns of water are probed. Therefore, even the unblended water lines with the lowest Einstein-A coefficient (e.g. at 12.565 μm , 20.662 μm , and 23.318 μm , as best seen in Fig. C2) are detectable. While there is general overlap between the retrievals, the full fit probes somewhat different temperatures and column densities, which is likely an effect of the non-LTE condition of ro-vibrational water. The smaller column density and temperature spread along the power laws might be a consequence of fitting many water lines of different origin. There are differences between the rotational water fit and the fit to the unblended water lines. The unblended lines retrieve a shallower relation between temperature and column density, resulting in higher column densities (by ~ 1 dex) at temperatures < 400 K and lower column densities (by ~ 1 dex) at temperatures > 600 K. This might be an effect of the composition upper level energies of the unblended lines. Due to the significant noise in line-free regions for this spectrum, we think that fitting the unblended water lines results in the most accurate description of H₂O emission conditions. However, despite of these differences, there seems to be a consensus of high columns of water that are dominated by warm temperatures (> 500 K) independent on the retrieval method. Analysing the water radial extent based on the fit to the unblended water lines, we find an inner and outer radius of 0.09 au and 0.18 au, respectively. Similar to CO, SiO, and CO₂ these values are broadly consistent with the radial position estimated based on line kinematics (Sect. 2.4).

The high column densities of (especially hot) water can be understood when comparing HD 35929 to other water-rich sources. BP Tau and XX Cha are found to have similar emitting areas (radial profiles up to radii of about ~ 2 au) and column densities ($\sim 10^{18} \text{ cm}^{-2}$) of their cold water component compared to HD 35929 (Temmink et al. 2025). In Appendix B, we highlight that the cold water lines in all three spectra look remarkably similar when scaled to the same distance. However, all hot water lines are systematically stronger for HD 35929 compared to the T Tauri discs. Therefore, the column densities at higher temperatures must be significantly larger in HD 35929

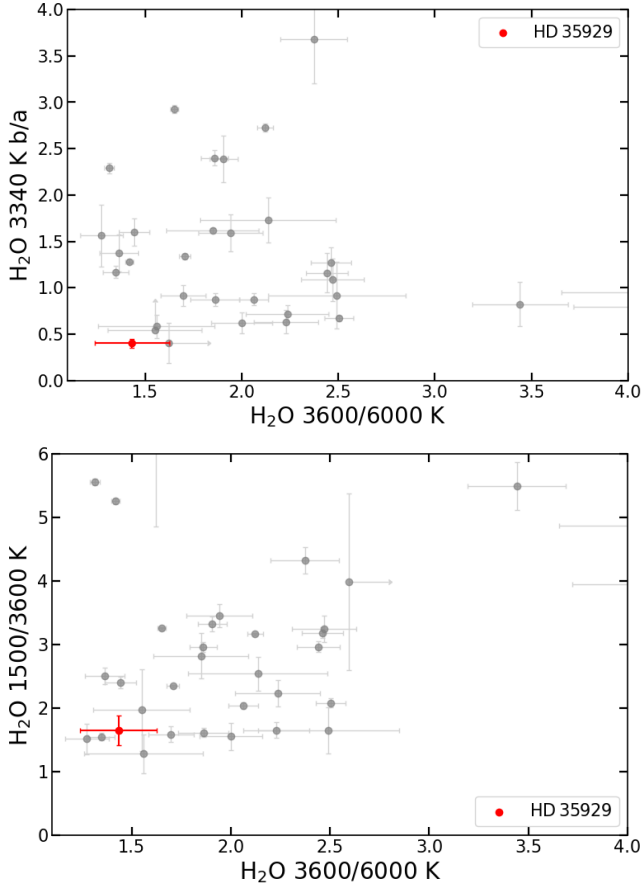


Figure 9. Water line diagnostics with the temperatures denoting the upper level energies (Banzatti et al. 2025). The x-axes show the ratio of water lines tracing warm water emission (~ 400 K) compared to hot water (~ 850 K). The vertical axis of the upper panel shows the ratio of two lines with similar upper level energies but different Einstein-A coefficients tracing the column densities of ~ 400 K water. The y-axis of the lower panel shows the ratio between water lines tracing cold emission (~ 200 K) and warm emission. The grey dots are observations taken by JWST/MIRI (Banzatti et al. 2025; Temmink et al. 2025) with the red dot indicating HD 35929.

than the column densities at high temperature found for BP Tau and XX Cha which are slightly larger than 10^{18} cm^{-2} . This is consistent with retrieved column densities above 10^{20} cm^{-2} .

Additionally, the conclusions regarding the column density and temperature can be tested without relying on models using the water line ratios introduced by Banzatti et al. (2025). The integrated line strengths were derived directly from the spectrum using iSLAT (Jellison et al. 2024). Fig. 9 shows the resulting line diagnostic diagrams. The column density tracer (H_2O 3340 K a/b) has a value of 0.40 which indicates high column densities and is very low compared to other objects observed by JWST/MIRI. Additionally, the low ratios of the cold/warm tracer (H_2O 1500/3600 K: 1.65) and warm/hot tracer (H_2O 3600/6000 K: 1.43) indicate an overall lack of cold water. This confirms model-independently the dominance of hot water with high column densities.

4 DISCUSSION

4.1 Presence of gas phase SiO

The visual evidence (Fig. 6) together with the Bayesian evidence presented in Sect. 3.2.3 leaves little doubt about the detection of gas phase SiO. The high excitation temperature and column density, combined with the width of the lines, strongly suggest a location very close to the star, near or within the silicate dust sublimation radius of HD 35929. To our knowledge, this is the first detection of ro-vibrational gas phase emission from SiO in a disc surrounding an intermediate-mass young star. Gas phase SiO has been suggested in the Spitzer spectrum of the young HD 172555 debris disc (Lisse et al. 2009); however, Johnson et al. (2012) questioned this, and a recent study by Samland et al. (2025) shows no evidence for gas phase SiO in the JWST/MIRI spectrum of that source.

Gas phase SiO is detected in molecular clouds and could play a role in the formation of silicates in cold environments (Reber et al. 2008; Krasnokutski et al. 2014; Yang et al. 2018; Rouillé et al. 2020). Gas phase SiO can also be produced in outflow or jet induced shocks that destroy silicate dust grains (Guilloteau et al. 1992; Bally 2016; Gusdorf et al. 2008). Gas phase SiO first overtone ro-vibrational line emission was found in dusty discs surrounding evolved luminous, massive B[e] supergiant stars (Kraus et al. 2015). These objects also show prominent CO ro-vibrational emission. Recently, gas phase SiO was detected in the fundamental ro-vibrational band towards two young protostars (Gelder et al. 2024). In these cases, the SiO is likely associated with shocks related to a disc wind or a jet, and it is not within the silicate dust sublimation radius. McClure et al. (2025) presented the detection of warm gas phase SiO in the innermost disc of a Class I protostar, where the high mass accretion rate causes the inner disc solids to evaporate. We note that no evidence for a jet in HD 35929 has been reported in the literature, but the type III P Cygni profiles detected in the UV point to an outflow (Grady et al. 1996). The [FeII] emission reported in Section 2.3 is blueshifted and may be formed in a lower density environment, possibly associated with the outflow detected in the UV. We checked that the SiO emission is not spatially extended.

We conclude that the SiO is probably associated with the high density, warm/hot inner disc, near or inside the dust sublimation radius. Under these conditions, SiO can be formed via a gas phase reaction between Si and OH, further leading to the formation of SiO_2 , which may condense into solid SiO_2 or other forms of silicates. The high column densities derived in Sect. 3.2.3 suggest that shielding by dust, and/or by molecules such as H_2O , and self-shielding may explain the survival of SiO close to this UV-bright star (Heays et al. 2017).

Chemical equilibrium models (e.g., GGChem, Woitke et al. 2018) show that in an oxygen-rich gas H_2O , CO, CO_2 , OH, and SiO form at high temperature and pressure; these are indeed the molecules we detect. However, when the formation of solids is taken into account, such chemical equilibrium models predict silicon to be depleted at temperatures below 1700 K (at 1 bar pressure), reaching a depletion of many orders of magnitude at temperatures below 1000 K, which is well above the retrieved temperature derived in Sect. 3.2.3 (Woitke et al. 2018). This suggests that the SiO is not fully condensing, indicating a non-equilibrium chemistry (which is not uncommon in protoplanetary discs as shown by Kanwar et al. 2025), or the derived SiO excitation temperature does not represent the true SiO gas kinetic temperature. In this context, it is interesting to note that Juhász et al. (2010) derived a high abundance of solid amorphous SiO_2 in HD 35929, as evidenced by the prominent 9.2-9.3 μm peak in the silicate emission, and the blue shoulder at about 8 μm .

4.2 Nature of the disc surrounding HD 35929

The MIRI spectrum of HD 35929 is remarkable because it is rich in molecular line emission. As mentioned in Section 1, previous observations of Herbig star discs using the Spitzer Space Telescope showed a low detection rate of molecular species compared to lower mass T Tauri stars (Pontoppidan et al. 2010). This was attributed to a bright dust continuum in Herbig stars and/or a modest spectral resolution and sensitivity (Antonellini et al. 2015) in combination with H₂O photodissociation by the strong stellar UV field (Fedele et al. 2011). Indeed, the SED of HD 35929 shows a steep spectral index at IR wavelengths, i.e. weak IR dust continuum emission. The dust is depleted in the smallest, (sub-) μm sized grains and lacks a substantial cold dust reservoir. In addition, the S/N of the HD 35929 MIRI data is very high (between 100 and 800). Therefore, the JWST/MIRI data of HD 35929 provide optimal conditions to detect the emission of molecules from its inner disc.

Near-IR interferometric observations of Herbig stars have revealed the presence of emission arising from close to, or within the (silicate) dust sublimation radius, which is pressure dependent and often taken at a temperature of 1500 K (Dullemond et al. 2001; Woitke et al. 2018). The nature of this emission has been debated. Eisner (2007) used the Keck Interferometer to spatially and spectrally resolve the inner disc of the Herbig star MWC 480 and found evidence for hot H₂O emission on a scale of 0.16 au. However, Najita et al. (2009) showed with high spectral resolution observations that MWC 480 lacks strong near-IR water line emission. Arulantham et al. (2025) presented JWST/MIRI MRS data of MWC 480 and found the presence of a compact warm H₂O reservoir (emitting area 0.2 au) with a column density of $10^{18.8} \text{ cm}^{-2}$. In addition, they report the presence of C₂H₂. The inner disc emission may also be due to hot refractory dust. Benisty et al. (2010) found strong inner disc emission from HD 163296 on spatial scales of 0.1 to 0.45 au, and attributed this to refractory dust species. The nature of the material in these innermost disc regions remains unclear, but our results for HD 35929 show that very dense and compact molecular gas reservoirs can exist on the spatial scales probed by the Keck and VLTI interferometers. In the light of this, the nature of the gas and dust in the inner 0.1 – 0.4 au of Herbig discs may need to be revisited.

However, the compact nature of the disc and the presence of high column density molecular gas emission set HD 35929 apart from other (Herbig) discs that lack such emission (Arulantham et al. 2025) (but see below) and tend to show colder dust reservoirs of material at larger distances from the star. HD 35929 shares some properties with that of the rapidly rotating 4 M_⊙ Herbig star 51 Oph (Ancker et al. 2001; Thi et al. 2005), with detections of CO, CO₂ and H₂O as well as silicate dust. The CO first overtone emission of 51 Oph is very compact, at a spatial scale of 0.1 au (GRAVITY Collaboration et al. 2021), i.e. comparable to that of HD 35929. The 2.5 M_⊙ Herbig star HD 101412 shows near-IR H₂O and OH as well as CO first overtone emission (Adams et al. 2019) and CO₂ emission (Pontoppidan et al. 2010), in a disc with a dust-depleted innermost region and prominent mid-IR dust emission from material at distances of the order of 2 au (Fedele et al. 2008). Adams et al. (2019) suggest the presence of a close-in planet separating the innermost dust depleted disc from the cooler material further out. The HD 35929 disc may represent a further evolutionary phase in the dispersal of discs surrounding intermediate-mass stars, in which only the innermost dust depleted region remains.

The estimated disc lifetime of HD 35929 is only a few years (Sect. 2.1), based on the observed gas accretion rate, a gas-to-dust mass ratio of 100, and the solid mass reservoir of only 0.23 M_⊕

(Stapper et al. 2025b). The disc lifetime could be longer if the gas accretion rate is variable, or the gas-to-dust mass ratio is (much) higher than nominal. The unusually high column density of water and other molecules derived in this study indeed suggest that we can see deep into the disc, possibly as a result of dust depletion.

Grant et al. (2023a) noticed that a subset of Herbig stars, mostly of Group II (Meeus et al. 2001), show a similar disc lifetime problem. They propose that these Group II discs may have experienced efficient pebble drift, and we detect these discs when they are at the brink of dispersal. Alternatively, the mass accretion rate may be overestimated because of contributions from a disc wind (Grant et al. 2023a), or possibly a breakdown of the calibration of mass accretion rates from emission line diagnostics for higher-mass, warmer stars: the spatial scale of the Br γ emission in Herbig stars is consistent with an origin in a disk wind (GRAVITY Collaboration et al. 2024).

An alternative explanation for the unusual disc properties of HD 35929 is a post-main-sequence evolutionary status of the star (Miroshnichenko et al. 2004). In that scenario, the disc is the result of the injection of gas from the stellar photosphere into the disc, where it may viscously spread. If the gas density is high enough, molecules can form (Thi et al. 2005; Thi & Bik 2005) and eventually even dust. This would alleviate the disc lifetime problem. A possible mechanism for the formation of such a disc could be the combination of rapid rotation and pulsations, as is observed in more massive Be stars (Rivinius & Klement 2026).

We can compare the JWST/MIRI observations of HD 35929, which is located in Orion, to those of irradiated discs in the XUE sample in NGC6357 (Ramírez-Tannus et al. 2023, 2025; Frediani et al. 2025). The XUE stars are 1 – 2 Myrs old and most have masses between 2 and 3 M_⊙, i.e. comparable to HD 35929. The XUE discs show both Group I as well as Group II SEDs, and line emission from a range of molecular species, including CO, H₂O, OH, CO₂, and C₂H₂. The XUE sample shows that the inner discs surrounding irradiated young intermediate-mass stars share gas and dust properties with lower mass discs in low mass star-forming regions. In one object, XUE10, very high CO₂ molecular gas column densities were found (Frediani et al. 2025). However, most of the XUE sample discs show relatively weak molecular line emission, suggesting inner disc gas column densities that are lower than found for HD 35929. This is in line with the small sample of Herbig stars observed using JWST/MIRI (Arulantham et al. 2025). Clearly, the high sensitivity of JWST is needed to detect warm inner-disc gas in discs surrounding Herbig stars. More JWST observations of discs surrounding intermediate-mass stars in different irradiation environments are needed to establish their inner disc molecular reservoir, placing HD 35929 into context.

4.3 Limitations of the model

Since the chosen modelling approach uses spectral templates, and is not based on a full thermochemical disc model, the resulting column densities cannot easily be translated into relative volume densities of the molecules probed since the molecules are not necessarily co-spatial. In addition, LTE was assumed in deriving the temperatures, which is likely not the case given the strong UV field of the star and the effects of IR pumping of the lines (e.g. Gelder et al. 2024). We have also neglected possible radiative transfer effects that could occur in discs with low dust opacities, in which the layers from which the gas and dust emission originate may be co-spatial, resulting in more complex spectra than can be allowed for in our models. In addition, the estimation of the dust continuum may result in neglecting optically thick gas pseudo-continuum emission, which would lead to

an underestimate of the gas column densities. Clearly, a next step in the analysis of the MIRI data needs to involve a full thermochemical disc model.

5 CONCLUSIONS

We have analysed the JWST/MIRI MRS spectrum of the Herbig star HD 35929, observed in the context of the MINDS (Kamp et al. 2023; Henning et al. 2024) program. The main findings of our study can be summarized as follows:

- We find a rich molecular line emission spectrum, dominated by warm/hot water, on top of a dust continuum with weak silicate emission bands. We also detect CO, CO₂, OH, SiO, HI and [FeII]. The continuum flux of the MIRI and Spitzer spectra show modest differences, indicating that the disc is relatively stable over a ~ 20 year time span.
- Many of the emission lines are spectrally resolved, placing the gas emission near the star at a typical distance of 0.1-0.2 au, close to or inside the dust sublimation radius of 0.4 au.
- We have fitted the continuum subtracted spectrum with DuCK-LinG, and find high column densities of water, and a clear lack of a cold water reservoir. Taken together with the very low mass and small size (< 17 au, (Stapper et al. 2025b) of the cold dust mass reservoir, the steeply declining SED, and the small angular scale observed in interferometric studies, we suggest that the disc is compact.
- The detected gas phase SiO emission likely originates from the inner disc. The derived SiO excitation temperatures are significantly below the condensation temperature of SiO, pointing to non-equilibrium chemistry or an underestimate of the SiO kinetic temperature.
- The nature of the HD 35929 disc is unclear. Its estimated lifetime is only a few years, which is incompatible with the persistent IR emission over longer timescales, yet it is clearly gas-rich. A significant fraction of Herbig stars have short lifetimes (Grant et al. 2023a), but not as short as HD 35929. We may be witnessing the final dispersal of a luminous ($\sim 70 L_{\odot}$) Herbig star disc, with only a small, gas-rich and dust-poor innermost disc remaining.

ACKNOWLEDGEMENTS

It is a pleasure to thank H. van Winckel, C. Aerts, N. van Assen, Th. Postma, Jelke Bethlehem, and the XUE team, lead by M.-C. Ramirez-Tannus and A. Bik for valuable discussions concerning the nature of HD 35929. We thank A. Banzatti for providing the iSHELL CO observations of HD 35929.

This work is based on observations made with the NASA/ESA/CSA James Webb Space Telescope. The data were obtained from the Mikulski Archive for Space Telescopes at the Space Telescope Science Institute, which is operated by the Association of Universities for Research in Astronomy, Inc., under NASA contract NAS 5-03127 for JWST. These observations are associated with program #1282. The following National and International Funding Agencies funded and supported the MIRI development: NASA; ESA; Belgian Science Policy Office (BELSPO); Centre Nationale d'Etudes Spatiales (CNES); Danish National Space Centre; Deutsches Zentrum für Luft- und Raumfahrt (DLR); Enterprise Ireland; Ministerio De Economía y Competitividad; Netherlands Research School for Astronomy (NOVA); Netherlands Organisation for Scientific Research (NWO); Science and Technology Facilities Council; Swiss Space Office; Swedish National Space Agency; and UK Space Agency.

T.K. acknowledges support from STFC Grant ST/Y002415/1.

M.T. acknowledges support from the ERC grant 101019751 MOLDISK.

E.v.D. acknowledges support from the ERC grant 101019751 MOLDISK and the Danish National Research Foundation through the Center of Excellence “InterCat” (DNRF150). I.K., A.M.A., and E.v.D. acknowledge support from grant TOP-1 614.001.751 from the Dutch Research Council (NWO).

T.H. and K.S. acknowledge support from the European Research Council under the Horizon 2020 Framework Program via the ERC Advanced Grant Origins 83 24 28.

A.C.G. acknowledges support from PRIN-MUR 2022 20228JPA3A “The path to star and planet formation in the JWST era (PATH)” funded by NextGeneration EU and by INAF-GoG 2022 “NIR-dark Accretion Outbursts in Massive Young stellar objects (NAOMY)” and Large Grant INAF 2022 “YSOs Outflows, Disks and Accretion: towards a global framework for the evolution of planet forming systems (YODA)”.

I.K. acknowledges funding from H2020-MSCA-ITN-2019, grant no. 860470 (CHAMELEON).

G.P. gratefully acknowledges support from the Carlsberg Foundation, grant CF23-0481 and from the Max Planck Society.

L.M.S. has received funding from the European Research Council (ERC) under the European Union’s Horizon 2020 research and innovation programme (PROTOPLANETS, grant agreement No. 101002188).

BT acknowledges to support of the Programme National PCMI of CNRS/INSU with INC/INP cofunded by CEA and CNES.

DATA AVAILABILITY

The analysed JWST/MIRI-MRS spectrum will be made public on the MINDS webpage (<https://minds.cab.inta-csic.es>). The DuCKLinG modelling setup can be found on github (<https://github.com/tillkaeufer/DuCKLinG>). Additional data products are available from the authors upon reasonable request.

REFERENCES

- Acke B., Bouwman J., Juhász A., Henning T., van den Ancker M. E., Meeus G., Tielens A. G. G. M., Waters L. B. F. M., 2010, *ApJ*, **718**, 558
- Adams S. C., Ádámkóvics M., Carr J. S., Najita J. R., Brittain S. D., 2019, *ApJ*, **871**, 173
- Ancker M. E. v. d., Meeus G., Cami J., Waters L. B. F. M., Waelkens C., 2001, *A&A*, **369**, L17
- Antonellini S., 2016, PhD thesis, University of Groningen, Netherlands
- Antonellini S., et al., 2015, *A&A*, **582**, A105
- Arabhavi A. M., et al., 2024, *Science*, **384**, 1086
- Arabhavi A. M., et al., 2025, *A&A*, **699**, A194
- Argyriou I., et al., 2023, *A&A*, **675**, A111
- Arulanantham N., et al., 2025, *AJ*, **170**, 67
- Bally J., 2016, *ARA&A*, **54**, 491
- Banzatti A., Garufi A., Kama M., Benisty M., Brittain S., Pontoppidan K. M., Rayner J., 2018, *A&A*, **609**, L2
- Banzatti A., et al., 2022, *AJ*, **163**, 174
- Banzatti A., et al., 2023, *AJ*, **165**, 72
- Banzatti A., et al., 2025, *AJ*, **169**, 165
- Barceló Forteza S., Moya A., Barrado D., Solano E., Martín-Ruiz S., Suárez J. C., García Hernández A., 2020, *A&A*, **638**, A59
- Benisty M., et al., 2010, *A&A*, **511**, A74
- Blake G. A., Boogert A. C. A., 2004, *ApJ*, **606**, L73
- Brittain S. D., Simon T., Najita J. R., Rettig T. W., 2007, *ApJ*, **659**, 685

- Brittain S. D., Najita J. R., Carr J. S., Ádámkóvics M., Reynolds N., 2016, *ApJ*, **830**, 112
- Brittain S. D., Kamp I., Meeus G., Oudmaijer R. D., Waters L. B. F. M., 2023, *Space Sci. Rev.*, 219, 7
- Buchner et al., 2014, *A&A*, 564, A125
- Buldryeva J., Yurchenko S. N., Tennyson J., 2022, *RAS Techniques and Instruments*, 1, 43
- Bushouse H., et al., 2024, JWST Calibration Pipeline, doi:10.5281/zenodo.14153298
- Calvet N., Muzerolle J., Briceño C., Hernández J., Hartmann L., Saucedo J. L., Gordon K. D., 2004, *AJ*, **128**, 1294
- Carnall A. C., 2017, *arXiv e-prints*, p. arXiv:1705.05165
- Carr J. S., Najita J. R., 2014, *ApJ*, 788, 66
- Colmenares M. J., et al., 2024, *ApJ*, 977, 173
- Dullemond C. P., Dominik C., Natta A., 2001, *ApJ*, **560**, 957
- Eisner J. A., 2007, *Nature*, 447, 562
- Fairlamb J. R., Oudmaijer R. D., Mendigutía I., Ilee J. D., van den Ancker M. E., 2015, *MNRAS*, **453**, 976
- Fedele D., et al., 2008, *A&A*, 491, 809
- Fedele D., Pascucci I., Brittain S., Kamp I., Woitke P., Williams J. P., Dent W. R. F., Thi W. F., 2011, *ApJ*, 732, 106
- Fedele D., van Dishoeck E. F., Kama M., Bruderer S., Hogerheijde M. R., 2016, *A&A*, **591**, A95
- Feroz F., Hobson M. P., 2008, *MNRAS*, 384, 449–463
- Feroz F., Hobson M. P., Bridges M., 2009, *MNRAS*, 398, 1601–1614
- Feroz F., Hobson M. P., Cameron E., Pettitt A. N., 2019, *The Open Journal of Astrophysics*, 2
- Frediani J., et al., 2025, *A&A*, **701**, A14
- GRAVITY Collaboration et al., 2019, *A&A*, **632**, A53
- GRAVITY Collaboration et al., 2021, *A&A*, **645**, A50
- GRAVITY Collaboration et al., 2024, *A&A*, 684, A43
- Gaia Collaboration 2020, *VizieR Online Data Catalog*, p. I/350
- Gasman D., et al., 2023, *A&A*, **679**, A117
- Gelder M. L. v., et al., 2024, *A&A*, 692, A197
- Gordon I. E., et al., 2022, *J. Quant. Spectrosc. Radiative Transfer*, **277**, 107949
- Grady C. A., et al., 1996, *A&AS*, **120**, 157
- Grant S. L., Espaillat C. C., Brittain S., Scott-Joseph C., Calvet N., 2022, *ApJ*, **926**, 229
- Grant S. L., Stapper L. M., Hogerheijde M. R., van Dishoeck E. F., Brittain S., Vioque M., 2023a, *AJ*, 166, 147
- Grant S. L., et al., 2023b, *ApJ*, 947, L6
- Guest E. R., Tennyson J., Yurchenko S. N., 2024, *Journal of Molecular Spectroscopy*, 401, 111901
- Guilloteau S., Bachiller R., Fuente A., Lucas R., 1992, *A&A*, **265**, L49
- Gusdorf A., Cabrit S., Flower D. R., Pineau Des Forêts G., 2008, *A&A*, 482, 809
- Heays A. N., Bosman A. D., Dishoeck E. F. v., 2017, *A&A*, 602, A105
- Hein Bertelsen R. P., Kamp I., van der Plas G., van den Ancker M. E., Waters L. B. F. M., Thi W. F., Woitke P., 2016, *A&A*, **590**, A98
- Henning T., et al., 2024, *PASP*, 136, 054302
- Herbig G. H., 1960, *ApJS*, 4, 337
- Ilee J. D., Fairlamb J., Oudmaijer R. D., Mendigutía I., van den Ancker M. E., Kraus S., Wheelwright H. E., 2014, *MNRAS*, 445, 3723
- Jellison E. G., Banzatti A., Johnson M. B., Bruderer S., 2024, *AJ*, **168**, 99
- Johnson B. C., et al., 2012, *ApJ*, 761, 45
- Juhász A., et al., 2010, *ApJ*, **721**, 431
- Kaeufer T., Min M., Woitke P., Kamp I., Arabhavi A. M., 2024a, *A&A*, **687**, A209
- Kaeufer T., Woitke P., Kamp I., Kanwar J., Min M., 2024b, *A&A*, **690**, A100
- Kamp I., et al., 2023, *Faraday Discussions*, 245, 112
- Kanwar J., Woitke P., Kamp I., Rimmer P., Helling C., 2025, *A&A*, **698**, A294
- Krasnokutski S. A., Rouillé G., Jäger C., Huisken F., Zhukovska S., Henning T., 2014, *ApJ*, 782, 15
- Kraus M., Oksala M. E., Cidale L. S., Arias M. L., Torres A. F., Fernandes M. B., 2015, *ApJ*, 800, L20
- Kurucz R. L., 1979, *ApJS*, **40**, 1
- Lazareff B., et al., 2017, *A&A*, 599, A85
- Lisse C. M., Chen C. H., Wyatt M. C., Morlok A., Song I., Bryden G., Sheehan P., 2009, *ApJ*, 701, 2019
- Malfait K., Waelkens C., Waters L. B. F. M., Vandenbussche B., Huygen E., de Graauw M. S., 1998, *A&A*, **332**, L25
- Marconi M., Ripepi V., Alcalá J. M., Covino E., Palla F., Terranegra L., 2000, *A&A*, **355**, L35
- McClure M. K., et al., 2025, *Nature*, 643, 649
- Meeus G., Waters L. B. F. M., Bouwman J., van den Ancker M. E., Waelkens C., Malfait K., 2001, *A&A*, **365**, 476
- Menu J., van Boekel R., Henning T., Leinert C., Waelkens C., Waters L. B. F. M., 2015, *A&A*, **581**, A107
- Miroshnichenko A. S., Gray R. O., Klochkova V. G., Bjorkman K. S., Kuratov K. S., 2004, *A&A*, 427, 937
- Najita J. R., Doppmann G. W., Carr J. S., Graham J. R., Eisner J. A., 2009, *ApJ*, 691, 738
- Perotti G., et al., 2023, *Nature*, **620**, 516
- Pontoppidan K. M., Salyk C., Blake G. A., Meijerink R., Carr J. S., Najita J., 2010, *ApJ*, 720, 887
- Pontoppidan K. M., et al., 2024, *ApJ*, 963, 158
- Ramírez-Tannus M. C., et al., 2023, *ApJ*, **958**, L30
- Ramírez-Tannus M. C., et al., 2025, *A&A*, **701**, A139
- Reber A. C., Paranthaman S., Clayborne A. Z., Khanna S. N., Castleman A. W. J., 2008, *ACS Nano*, 2, 1729
- Rivinius T., Klement R., 2026, in *Encyclopedia of Astrophysics*. pp 430–448 (arXiv:2411.06882), doi:10.1016/B978-0-443-21439-4.00042-0
- Romero-Mirza C. E., et al., 2024, *ApJ*, **975**, 78
- Rouillé G., Jäger C., Henning T., 2020, *ApJ*, **892**, 96
- Salyk C., et al., 2025, *AJ*, **169**, 184
- Samland M., et al., 2025, *ApJ*, **989**, 132
- Sargent B. A., et al., 2008, *ApJ*, 690, 1193
- Stapper L. M., Hogerheijde M. R., van Dishoeck E. F., Booth A. S., Grant S. L., van Terwisga S. E., 2025a, *A&A*, **693**, A49
- Stapper L. M., Hogerheijde M. R., van Dishoeck E. F., Vioque M., Williams J. P., Ginski C., 2025b, *A&A*, **693**, A286
- Tabone B., et al., 2023, *Nature Astronomy*, 7, 805
- Tabone B., Dishoeck E. F. v., Black J. H., 2024, *A&A*, 691, A11
- Temminck M., et al., 2024a, *A&A*, **686**, A117
- Temminck M., et al., 2024b, *A&A*, 689, A330
- Temminck M., et al., 2025, *A&A*, **699**, A134
- Tennyson J., et al., 2024, *J. Quant. Spectrosc. Radiative Transfer*, **326**, 109083
- Thi W. F., Bik A., 2005, *A&A*, **438**, 557
- Thi W. F., van Dalen B., Bik A., Waters L. B. F. M., 2005, *A&A*, **430**, L61
- Trotta R., 2008, *Contemporary Physics*, 49, 71
- Valegård P. G., Waters L. B. F. M., Dominik C., 2021, *A&A*, **652**, A133
- Valenti J. A., Johns-Krull C. M., Linsky J. L., 2000, *ApJS*, 129, 399
- Vines J. I., Jenkins J. S., 2022, *MNRAS*, 513, 2719
- Vioque M., Oudmaijer R. D., Baines D., Mendigutía I., Pérez-Martínez R., 2018, *A&A*, **620**, A128
- Vioque M., et al., 2023, *AJ*, **166**, 183
- Wichitanakom C., Oudmaijer R. D., Fairlamb J. R., Mendigutía I., Vioque M., Ababakr K. M., 2020, *MNRAS*, 493, 234
- Wilson T. L., 1999, *Reports on Progress in Physics*, **62**, 143
- Woitke P., Helling C., Hunter G. H., Millard J. D., Turner G. E., Worters M., Bleic J., Stock J. W., 2018, *A&A*, 614, A1
- Woitke P., Thi W. F., Arabhavi A. M., Kamp I., Kóspál Á., Ábrahám P., 2024, *A&A*, **683**, A219
- Woods P. M., Willacy K., 2009, *ApJ*, **693**, 1360
- Wright G. S., et al., 2023, *PASP*, 135, 048003
- Yang T., Thomas A. M., Dangi B. B., Kaiser R. I., Mebel A. M., Millar T. J., 2018, *Nature Communications*, 9, 774
- van der Plas G., van den Ancker M. E., Fedele D., Acke B., Dominik C., Waters L. B. F. M., Bouwman J., 2008, *A&A*, 485, 487

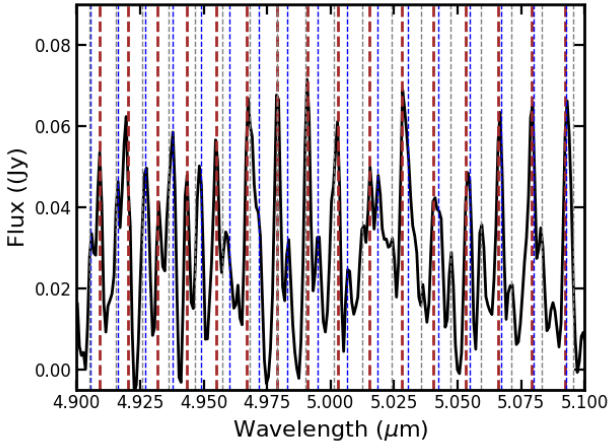


Figure A1. CO ro-vibrational emission lines in HD 35929. The dashed lines indicate the positions of the $v=1-0$ (red), $v=2-1$ (blue) and $v=3-2$ (grey) rotational lines. The observed spectrum has been corrected for the radial velocity of the star of 22 km/s.

APPENDIX A: CO RO-VIBRATIONAL LINE EMISSION

In Fig. A1 we show the continuum subtracted MIRI spectrum of HD 35929 between $4.9\ \mu\text{m}$ and $5.1\ \mu\text{m}$. This region shows CO emission that is significantly broadened and blended as discussed in Sect. 2.4.

APPENDIX B: COMPARING HD 35929 TO WATER-RICH T TAURI DISCS

This section compares the rotational water spectrum of HD 35929 to the spectra of the water-rich T Tauri discs of BP Tau and XX Cha (Temmink et al. 2025) which we show to be cold-water analogues. The spectra are both scaled to the distance of HD 35929 (380 pc) and selected wavelength windows are compared in Fig. B1. The cold water lines look remarkably similar for all objects. This includes the coldest water lines (upper level energies of less than 2000 K) around $23.82\ \mu\text{m}$ and $23.90\ \mu\text{m}$, but also the unblended water line at $17.36\ \mu\text{m}$. The only exception seems to be the unblended line at $17.57\ \mu\text{m}$, which is roughly a factor of 2 stronger in HD 35929. Unblended warm water lines (e.g. at $17.10\ \mu\text{m}$ and $17.50\ \mu\text{m}$) also exhibit strong similarities, especially for BP Tau. The relative enhancement of cold water lines compared to warm water lines of XX Cha have been noted by Temmink et al. (2025) already. We conclude that the emitting conditions of the cold (and warm) water reservoirs must be very similar between all objects.

Temmink et al. (2025) fitted BP Tau and XX Cha with a temperature and column density power law (among other profiles) allowing for a direct comparison between the retrieved conditions and HD 35929. The profiles of both discs extend outwards to ~ 2.0 au with near constant column densities of $10^{18}\ \text{cm}^{-2}$, which coincides extremely well with the cold water conditions retrieved for HD 35929 (see Fig. 8). However, as shown in Fig. B1, the unblended water lines with upper level energies above 6000 K, tracing the hot water component, are significantly stronger for HD 35929 (seen at $17.14\ \mu\text{m}$, $17.19\ \mu\text{m}$, $17.32\ \mu\text{m}$, and $17.60\ \mu\text{m}$). Additionally, most of the wavelength ranges between the unblended water lines which show significantly more flux for HD 35929 are dominated by blended lines with high upper level energies. This conclusively shows that the column

densities of hot water must be higher than the values retrieved by Temmink et al. (2025) for BP Tau and XX Cha ($\sim 10^{18}\ \text{cm}^{-2}$).

We note that even though many lines will be optically thick at their line centres, an increase in column density still results in an increase in line flux due to the increase in flux in the optically thin line wings. For example, a slab model with a temperature of 800 K shows an increase of flux at the hot water line at $17.32\ \mu\text{m}$ (Einstein-A coefficient of 41.53) by a factor of 1.87 when increasing the column density from $10^{18}\ \text{cm}^{-2}$ to $10^{19}\ \text{cm}^{-2}$.

APPENDIX C: FITTING THE ROTATIONAL WATER LINES

This section shows the fits to the rotational and unblended water lines. The fits are explained in Sect. 3.2.3. Fig. C1 shows the fit to the rotational water lines in the range of $13.5 - 25.0\ \mu\text{m}$ and Fig. C2 displays a fit to the unblended water lines between $11.7\ \mu\text{m}$ and $25.0\ \mu\text{m}$.

APPENDIX D: NON-DETECTIONS OF ISOTOPOLOGUES

Given the high retrieved column densities, naturally the question arises if isotopologues of the fitted molecules are visible in the spectrum as well. Therefore, we investigate the possibility of features by $^{13}\text{CO}_2$ and H_2^{18}O .

Multiple JWST/MIRI spectra of protoplanetary discs show a clear feature of $^{13}\text{CO}_2$ around $15.4\ \mu\text{m}$ (e.g. Grant et al. 2023b; Salyk et al. 2025). The spectrum of HD 35929 does not exhibit any sign of it (e.g. Fig. 4). If an abundance fraction of 70 is assumed between $^{12}\text{CO}_2$ and $^{13}\text{CO}_2$ (Woods & Willacy 2009) and line overlap between the isotopologues is taken into account, the model fitted to the spectrum (Fig. 4) would show a peak $^{13}\text{CO}_2$ line flux of 13.44 mJy, which would be detectable. We can only speculate regarding the reasons for the observed non-detection. $^{13}\text{CO}_2$ is optically thinner than $^{12}\text{CO}_2$ and therefore potentially traces deeper disc layers with lower temperatures. This effect has been observed by Grant et al. (2023b), with a temperature difference of 75 K. For the retrieved model, decreasing the temperature by 200 K results in peak fluxes of 6.88 mJy which even though significantly larger than the estimated noise by the JWST Exposure Time Calculator (ETC) at this wavelength (0.7 mJy) might result in a non-detection due to the uncertainties of the continuum subtraction and interference with other molecular features. Similarly, it is possible that the column density of $^{13}\text{CO}_2$ is lower than expected. This can be due to a lower $^{13}\text{CO}_2$ to $^{12}\text{CO}_2$ ratio or due to an overestimation of the $^{12}\text{CO}_2$ column density. As discussed in Section 3.2.3, fitting only the Q-branch results in lower column densities by approximately a factor of 10. Progressing this to $^{13}\text{CO}_2$ would result in a hard-to-detect peak flux of 4.74 mJy.

Water isotopologues are difficult to detect in JWST/MIRI spectra (Gasman et al. 2023; Temmink et al. 2024b), due to the strong overlap with water lines and the low isotopologue ratio ($^{16}\text{O}/^{18}\text{O}$ of 550, Wilson 1999). Salyk et al. (in prep.) identified several isolated H_2^{18}O lines that will assist with future detections. All lines are longwards of $22.7\ \mu\text{m}$ and have upper level energies below 3300 K. A visual inspection of the spectrum did not result in conclusive evidence for any H_2^{18}O line. However, at these long wavelengths the spectrum of HD 35929 is dominated by noise. At $24\ \mu\text{m}$ and $26\ \mu\text{m}$ the ETC estimated noise is 1.84 mJy and 3.89 mJy, respectively. Additional uncertainty sources like the continuum subtraction complicate the isotopologue detection further.

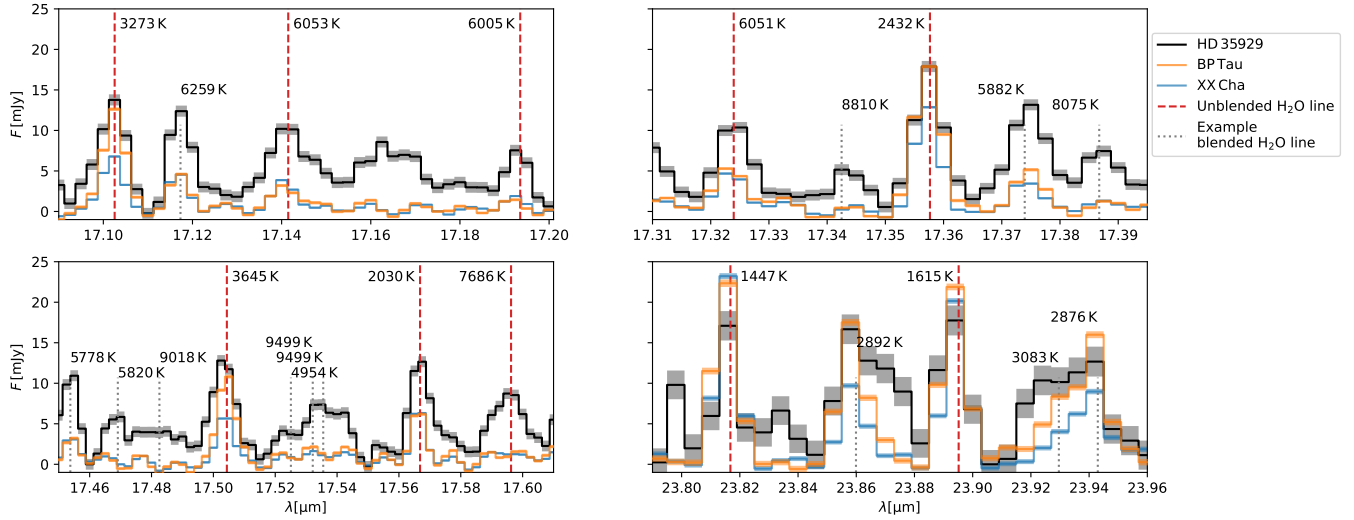


Figure B1. Selected wavelength windows showing the JWST/MIRI spectra of HD 35929 (black) and the two T Tauri discs BP Tau and XX Cha (orange and blue, [Temmink et al. 2025](#)), scaled to the same distance. A few unblended water lines (red, as identified by [Banzatti et al. 2025](#)) and examples of blended water lines (grey) are labelled with their upper level energy.

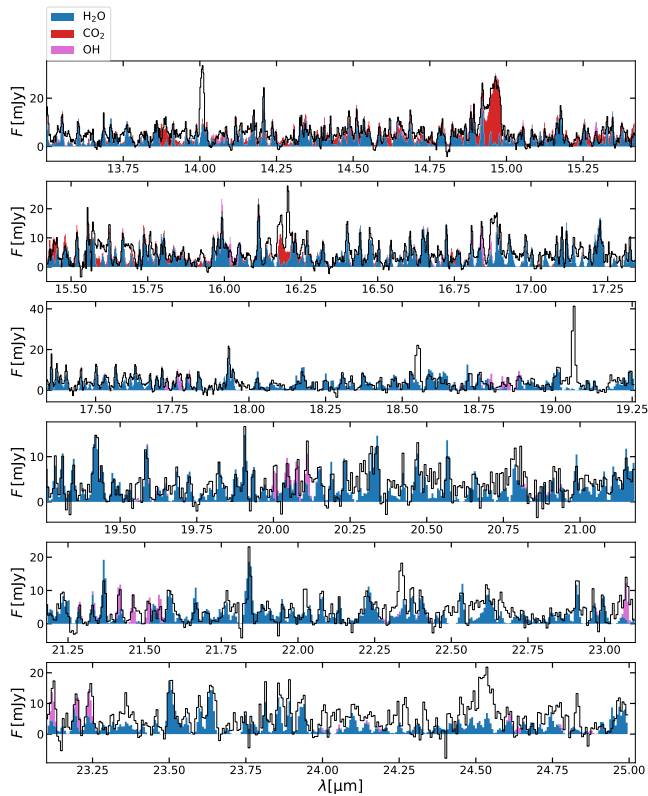


Figure C1. Fitting the rotational water lines in the continuum subtracted MIRI spectrum from 13.5 μm to 25.0 μm . Overplotted are the contributions of H₂O, CO₂, and OH from the median probability model.

APPENDIX E: MEASURED EMISSION LINES.

This paper has been typeset from a \LaTeX file prepared by the author.

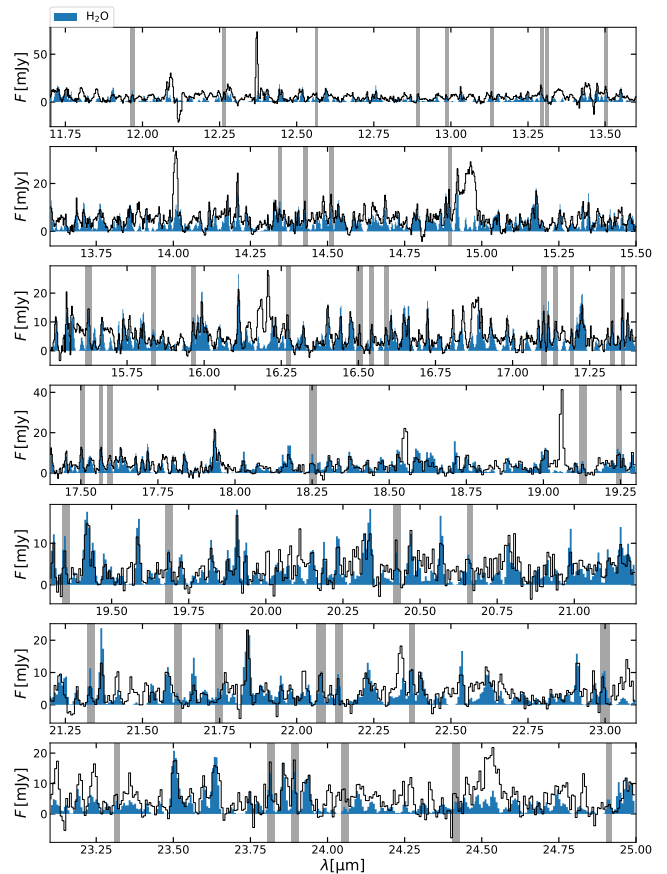


Figure C2. Fitting the unblended rotational water lines in the continuum subtracted MIRI spectrum. Overplotted is the contribution of H₂O from the median probability model. The shaded regions are the wavelength windows used during fitting.

Table E1. Measured data of selected molecular emission lines and strong HI recombination lines, using iSLAT. Given are the quantum levels of the upper and lower levels, the rest wavelength of the transition, the line flux and error from the Gaussian fit, the measured Full Width at Half Maximum (FWHM) and its error, corrected for the MIRI instrument spectral resolution, and the Doppler shift of the line, assuming a stellar radial velocity of 22 km/s.

Upper level	Lower level	Wavelength μm	Line flux	Line flux error	FWHM	FWHM error	Doppler shift
			$\text{erg}/\text{cm}^2 \text{ s}$		km/s		km/s
CO							
1	0 P-28	4.94336	1.64e-14	2.75e-15	115.1	27.3	-9.8
1	0 P-31	4.97878	2.59e-14	8.15e-16	135.7	5.3	3.1
2	1 P-26	4.98310	1.41e-14	2.42e-15	196.1	34.9	-21.4
3	2 P-26	5.04724	9.69e-15	1.36e-15	125.4	22.7	-14.7
3	2 P-27	5.05907	1.62e-14	2.60e-15	194.8	31.5	11.9
1	0 P-49	5.21766	1.37e-14	5.38e-15	303.5	115.2	-15.1
1	0 P-52	5.26221	6.02e-15	7.23e-16	85.4	18.5	-10.4
SiO v=1-0							
56	55	7.72822	6.47e-15	1.38e-15	215.4	42.1	-197.9
44	43	7.79399	3.47e-15	3.63e-16	76.7	13.9	-1.7
33	32	7.86396	1.14e-14	3.74e-15	263.3	78.2	7.0
36	35	7.84394	3.81e-15	4.42e-16	115.6	15.9	26.7
17	16	7.98289	5.70e-15	1.50e-15	133.0	38.0	3.5
6	5	8.07693	5.28e-15	5.37e-16	104.2	13.4	-8.4
8	9	8.22220	2.82e-15	5.93e-16	64.9	26.9	10.6
30	31	8.47350	4.59e-15	3.83e-16	143.8	11.9	-17.1
34	35	8.52443	4.55e-15	2.21e-15	219.1	102.2	-63.3
35	36	8.53742	5.15e-15	1.08e-15	192.2	36.9	-7.0
39	40	8.59049	5.14e-15	9.33e-16	129.2	24.4	13.2
OH							
X3/2_0 15.0	X3/2_0 RR_13.5ff_14.0	20.00854	8.55e-16	2.54e-16	100.5	61.0	-6.0
X3/2_0 15.0	X3/2_0 RR_13.5ee_14.0	20.04975	9.79e-16	3.91e-16	201.0	85.2	-25.5
X1/2_0 14.0	X1/2_0 RR_12.5ee_13.0	20.08194	8.69e-16	2.12e-16	88.6	51.5	-11.5
X3/2_0 14.0	X3/2_0 RR_12.5ff_13.0	21.41989	1.10e-15	1.09e-16	149.5	22.0	20.2
X1/2_0 13.0	X1/2_0 RR_11.5ee_12.0	21.51689	7.71e-16	3.22e-16	162.6	92.9	-26.1
HI							
n_{up}	n_{low}						
6	5	7.45988	3.47e-14	2.12e-15	125.1	8.0	-4.6
10	7	8.76006	1.11e-14	1.03e-15	131.0	12.5	13.3
6	5	7.45988	3.47e-14	2.04e-15	125.0	7.6	-4.6
10	7	8.76006	1.12e-14	1.20e-15	134.7	14.6	13.8
9	7	11.30869	6.58e-15	1.61e-16	141.0	4.2	-7.0
7	6	12.37192	1.07e-14	6.97e-16	113.7	10.9	2.7
10	8	16.20910	3.64e-15	2.44e-16	167.7	13.2	-5.7
8	7	19.06189	4.49e-15	3.94e-16	122.7	19.1	0.2
11	9	22.34046	2.75e-15	9.97e-17	287.1	10.0	-3.3

Table E1. continued.

Upper level $v_1 v_2 v_3$	Lower level $J_{K_a K_c}$	Wavelength μm	Line flux	Line flux error $\text{erg}/\text{cm}^2 \text{ s}$	FWHM	FWHM error km/s	Doppler shift km/s
H ₂ O							
010 2 ₂₁	000 2 ₁₂	6.01392	1.31e-14	2.54e-15	359.7	65.2	210.7
010 3 ₂₁	000 3 ₁₂	6.07545	6.18e-15	8.84e-16	193.6	26.3	14.6
010 1 ₀₁	000 1 ₁₀	6.34443	5.29e-15	3.75e-16	177.5	11.8	-1.6
010 5 ₃₂	000 6 ₄₃	7.27924	4.41e-15	4.24e-16	121.7	12.8	-24.2
010 5 ₃₃	000 6 ₄₂	7.30659	5.55e-15	3.28e-16	192.1	10.8	12.1
000 14 ₈₇	000 13 ₅₈	11.96812	1.28e-15	2.95e-16	122.4	42.5	13.9
000 18 ₇₁₂	000 17 ₄₁₃	12.26544	1.44e-15	2.06e-16	111.9	24.8	8.6
000 10 ₆₅	000 9 ₁₈	12.56450	1.68e-15	5.80e-16	186.4	75.0	-21.6
000 12 ₅₇	000 11 ₂₁₀	12.89409	1.21e-15	2.47e-16	127.6	31.6	21.6
000 12 ₇₅	000 11 ₄₈	12.98575	1.08e-15	2.50e-16	167.0	39.9	5.4
000 16 ₇₁₀	000 15 ₄₁₁	13.13243	1.27e-15	2.61e-16	128.3	31.1	-0.1
000 15 ₃₁₂	000 14 ₂₁₃	13.29319	2.81e-15	3.72e-16	190.4	24.6	0.7
000 16 ₄₁₂	000 15 ₃₁₃	13.31231	5.59e-16	2.04e-16	8.9	266.6	-10.5
000 11 ₇₄	000 10 ₄₇	13.50312	3.03e-15	2.25e-16	214.1	17.8	-5.3
000 14 ₃₁₁	000 13 ₂₁₂	14.34608	2.03e-15	7.45e-16	320.2	122.0	20.4
000 15 ₄₁₁	000 14 ₃₁₂	14.42757	1.28e-15	3.17e-16	102.6	41.7	-16.5
000 13 ₂₁₁	000 12 ₁₁₂	14.51301	2.39e-15	3.80e-16	213.8	34.5	-0.5
000 14 ₅₁₀	000 13 ₂₁₁	14.89513	1.89e-15	3.94e-16	133.7	35.4	-0.7
000 13 ₃₁₀	000 12 ₂₁₁	15.62568	2.25e-15	4.24e-16	210.9	41.4	-16.4
000 18 ₈₁₀	000 17 ₇₁₁	15.83495	8.64e-16	1.21e-16	221.6	34.0	32.2
000 13 ₅₉	000 12 ₂₁₀	15.96622	1.24e-15	1.75e-16	143.6	26.5	4.7
000 15 ₅₁₀	000 14 ₄₁₁	16.27136	1.51e-15	2.40e-16	153.7	29.7	3.1
000 17 ₇₁₀	000 16 ₆₁₁	16.50525	1.02e-15	3.57e-16	213.4	74.5	-24.0
000 11 ₆₆	000 10 ₃₇	16.54402	7.30e-16	1.12e-16	48.4	35.1	17.9
000 16 ₉₇	000 15 ₈₈	16.59123	9.77e-16	6.91e-17	161.2	13.3	-0.1
000 12 ₅₈	000 11 ₂₉	17.10254	1.17e-15	1.27e-16	97.7	17.1	-11.0
000 16 ₈₈	000 15 ₇₉	17.14148	1.38e-15	1.69e-16	199.6	25.9	1.6
010 13 ₄₉	010 12 ₃₁₀	17.19352	5.98e-16	7.29e-17	77.1	20.3	-16.0
000 16 ₈₉	000 15 ₇₈	17.32395	9.06e-16	9.77e-17	93.9	16.6	1.1
000 11 ₂₉	000 10 ₁₁₀	17.35766	1.18e-15	9.13e-17	47.4	15.3	-4.2
000 13 ₄₉	000 12 ₃₁₀	17.50436	1.30e-15	1.01e-16	135.2	12.8	-20.0
000 8 ₆₃	000 7 ₃₄	17.56683	1.13e-15	9.30e-17	106.4	12.7	0.4
010 15 ₇₈	010 14 ₆₉	17.59626	1.31e-15	1.00e-16	234.4	17.6	-17.2
000 11 ₅₇	000 10 ₂₈	18.25429	7.79e-16	2.68e-16	175.7	81.1	-19.6
000 11 ₃₈	000 10 ₂₉	19.24597	1.23e-15	1.14e-16	162.6	20.1	8.7
000 10 ₅₆	000 9 ₂₇	19.34995	6.99e-16	2.72e-16	62.7	103.3	16.1
000 14 ₇₈	000 13 ₆₇	19.68805	1.02e-15	3.38e-16	227.5	78.0	-9.0
000 13 ₇₇	000 12 ₆₆	20.42595	8.34e-16	2.73e-16	90.5	62.1	-3.3
000 7 ₄₃	000 6 ₁₆	20.66181	1.71e-15	1.15e-16	518.0	36.3	-79.6
000 12 ₇₆	000 11 ₆₅	21.33317	4.62e-16	7.63e-17	83.0	43.0	-5.2
000 11 ₄₇	000 10 ₃₈	22.08091	1.11e-15	1.12e-16	177.4	22.2	-3.6
000 11 ₇₄	000 10 ₆₅	22.37473	1.22e-15	1.19e-16	168.8	21.9	7.8
000 12 ₆₇	000 11 ₅₆	22.99881	6.15e-16	1.64e-16	64.3	66.6	-34.7
000 10 ₆₅	000 10 ₃₈	23.31846	5.79e-16	8.78e-17	123.2	30.4	-31.9
000 8 ₄₅	000 7 ₁₆	23.89518	1.23e-15	6.41e-17	87.6	10.4	-14.8
010 16 ₅₁₂	010 15 ₄₁₁	24.05845	1.10e-15	4.39e-16	300.3	122.3	-40.4
010 9 ₆₃	010 8 ₅₄	24.91403	3.98e-16	1.57e-16	268.3	137.1	-4.6